Studies on mechanisms of rabies virus infection, proliferation, and pathogenesis

（狂犬病ウイルスの感染増殖および病態発現機構に関する研究）

Yukari Itakura

Contents

Chapter II:
Morphogenesis of bullet-shaped rabies virus particles requires a functional interplay between the viral matrix protein and ESCRT-I component TSG101

Abbreviations

ACSA2: Astrocyte cell surface antigen-2

BHK/T7-9 cell: Baby hamster kidney cells stably expressing T7 RNA polymerase

BSA: Bovine serum albumin

BW: body weight

CNS: Central nervous system

CVS strain: Challenge virus standard strain

DMEM: Dulbecco's Modified Eagle's Medium

dpi: Days post infection

ELISA: Enzyme-linked immune sorbent assay

EMEM: Eagle's Minimum Essential Medium

ERA strain: Evelyn-Rokitnicki-Abelseth strain

ESCRT: Endosomal sorting complex required for transport

FBS: Fetal bovine serum

ffu: Focus forming unit

FITC: Fluorescein isothiocyanate

FSC: Forward scatter

G333: Amino acid position 333 in the glycoprotein

GFAP: Glial fibrillary acidic protein

G: Glycoprotein

HEP strain: High egg passage Flury strain

hpi: Hours post infection

Iba1: Ionized calcium-binding adapter molecule 1

IFIT2: Interferon induced protein with tetratricopeptide repeats 2

IFN: Interferon

IGR: Intergenic region

IRF3: Interferon regulatory factor 3

ISG: IFN-stimulated gene

KD: Knockdown

KO: Knockout

L: Large protein

L-domain: Late-domain

M: Matrix protein

MAP2: Microtubule-associated protein 2

MOI: Multiplicity of infection

NeuN: Neuronal nuclei

N: Nucleoprotein

OAS: Oligoadenylate synthase

ORF: Open reading frame

OIE: International Epizootic Office

p75NTR: Low-affinity nerve growth factor (NGF) receptor

P: Phosphoprotein

PB: Phosphate buffer

PBS: Phosphate-buffered saline

PBST: PBS with 0.01% Tween-20

pHEP: a plasmid vector carrying the full-length cDNA of HEP strain

qRT-PCR: Quantitative reverse transcription polymerase chain reaction

RABV: Rabies virus

RNP: Ribonucleoprotein

rpm: Rotations per minute

rRABV: Recombinant rabies virus

SD: Standard deviation

SSC: Side scatter

STAT1: Signal transducers and activator of transcription-1

SVG-A cell: Simian virus 40 (SV40)-transformed human fetal astrocyte derived cell

TSG101: Tumor susceptibility gene 101

VSV: Vesicular stomatitis virus

WHO: World Health Organization

WT: Wild type

Publications

Chapter I

Itakura, Y. *et al.* Glu_{333} in rabies virus glycoprotein is involved in virus attenuation through astrocyte infection and interferon responses. *iScience* **25**, 104122 (2022).

Preface

Rabies virus (RABV) is a well-recognized zoonotic virus that causes rabies; a fatal neurological disease in mammals. Rabies is distributed almost all over the world and, at least 59,000 human deaths are estimated annually, particularly in Asian and African countries[1]. Dogs are the major source of RABV infection in these countries[2]. Approximate 99% of human rabies cases are caused by virus transmission through a bite by a rabid dog[3]. Therefore, resolving the virus spread among dogs is considered one of the most important challenges in rabies control. Besides, in today's global society, everyone is at risk of rabies by a contact with wildlife or imported animals[4–7]. Because of its global impact, rabies is a notifiable disease to the World Health Organization (WHO) and World Organization for Animal Health (WOAH) [1,8].

Once clinical signs of rabies have appeared, almost all patients will be fatal. One of the critical challenges of rabies is that there is no effective treatment for rabies. On the other hand, vaccines against rabies are invariably effective, even after an exposure to RABV with proper post exposure prophylaxis. However, because of the low availability and low quality of the locally-manufactured vaccines in addition to difficulties in controlling stray dog population, rabies remains as a considerable public health problem in local communities in developing countries[2].

The saliva of RABV-infected animals usually contains large amounts of RABV, and the virus is transmitted to new hosts through bite wounds[9]. RABV is thought to invade peripheral nerve fibers and to ascend afferently to the central nerves system (CNS)[10,11]. Before reaching the CNS, RABV migrates slowly to escape from the host's immune response; so-called incubation period, which could vary from a week to a year depending on the distance from the bite site to CNS[2]. Once RABV reaches the CNS, it multiplies dramatically and causes neurological symptoms in the host. There are furious and paralytic form of rabies and both eventually lead to death within a week from the disease onset[2]. It has been suggested that the neurological symptoms induced by RABV infection could be due to mitochondrial disorders, dysfunction of ion channels, or neurotransmission rather than the neuronal cell death or degeneration[12–15]. However, how RABV replicates to manifest fatal virulence has not been fully clarified.

RABV, belonging to the genus *Lyssavirus* of the family *Rhabdoviridae* in the order *Mononegavirales*, possesses a negative-sense single-stranded RNA genome. This genome encodes five viral proteins: the nucleoprotein (N), phosphoprotein (P), matrix protein (M),

glycoprotein (G), and large protein (L)[16]. Each open reading frame (ORF) is flanked by transcription initiation and stop signals, and intergenic regions (IGRs) exist between each ORF. Viral genome is neatly surrounded by RABV N. Viral RNA-N complex is a main component of ribonucleoprotein (RNP) complex together with RABV L and P, which are a RNA-dependent RNA polymerase and a functional co-factor of RABV L, respectively. RABV L can process as both transcription and replication of viral genome. RABV P is involved in the stabilization of RABV L and has a role to bridge RABV L and viral RNA-N. Furthermore, RABV P has also been reported to inhibit the host innate immune response by inhibiting nuclear translocation of interferon (IFN)-regulatory factor 3 (IRF3) and signal transducer and activator of transcription 1 (STAT1)[14,17–19]. The RNP complex is organized in a helical structure and forms the basis of the bullet shape. The RNP buds from the host lipid membrane as an enveloped bullet-shaped virus particle. RABV M is a viral protein present between the envelope and RNP[20]. It is believed to contribute to RNP structure retention and viral budding, while also being responsible for RABV L transcription/replication switching[20,21]. RABV G forms a trimer and exists on the envelope toward outside, binds to the receptors and triggers infection, and is one of the important virulence determinants as well[16,20].

Rabies is one of the neglected tropical diseases, and no effective treatment has been established although it is one of the oldest known and fatal infectious diseases. Gaining knowledge about detail mechanism of RABV infection can be the basis of vaccine improvement and therapeutics development. In this study, an attempt was made to clarify the mechanism of RABV infection, proliferation, and pathogenicity on the aspects of virus and host factors. Chapter I focused on viral factor that determines the pathogenicity of RABV infection. The study analyzed the attenuation mechanism of the RABV vaccine strain, which depends on a single amino acid mutation in the viral protein, revealing that astrocytic tropism and IFN responses in astrocytes influence RABV virulence. Chapter II then focused on host factors involved in RABV infection and proliferation. Tumor susceptibility gene 101 protein (TSG101) was identified as a host factor contributing RABV infection, and a functional interplay between RABV and TSG101 to promote RABV budding and particle formation was clarified.

Chapter I:

Attenuation of rabies virus defined by amino acid 333 of the G protein is associated with astrocyte infection and subsequent interferon responses

Summary

The amino acid residue at position 333 of the RABV G (G333) is a major determinant of RABV pathogenicity. Mostly, virulent RABV strains possess Arg_{333}, whereas the attenuated strain High egg passage Flury (HEP) possesses Glu_{333}. To investigate the potential attenuation mechanism dependent on a single amino acid at G333, comparative analysis was performed between HEP and $HEP^{333}R$ mutant with Arg_{333} instead of Glu_{333}. Their respective tropism for astrocytes and the subsequent immune responses in astrocytes were examined. Virus replication and subsequent IFN responses in astrocytes infected with HEP increased compared with $HEP^{333}R$ both *in vitro* and *in vivo*. Furthermore, involvement of IFN in the avirulency of HEP was demonstrated in IFN-receptor knockout mice. These results indicate that Glu_{333} contributes to RABV attenuation by determining the ability of the virus to infect astrocytes and stimulate subsequent IFN responses.

Introduction

Highly pathogenic strains of RABV often exhibit characteristics related to their strict neurotropism [22–24]. In contrast, attenuated strains often exhibit a broader cell tropism not specific to neuronal cells *in vitro* and show limited ability to spread to the CNS *in vivo* [25,26]. Among the viral proteins, the RABV G exists as a trimer on the surface of the RABV virion. Because RABV G is responsible for host cell receptor recognition[27–30] and membrane fusion [31], mutations in the RABV G often alter viral pathogenicity. In particular, a basic amino acid at G333 such as Arg_{333} or Lys_{333} contributes to virulence in some fixed strains of RABV in adult mice [32–36]. To understand this property, several studies have attempted to characterize the role of the amino acid at G333. An amino acid substitution for Glu_{333} enhanced viral-induced apoptosis in infected cells, leading to a loss of pathogenicity in mice [25]. Infection with recombinant RABV artificially encoding dual RABV G with Glu_{333} also resulted in enhanced apoptosis in cells [37]. One study has reported that amino acid at G333 influences the binding affinity of RABV G to one of the receptors for RABV, low-affinity nerve growth factor (NGF) receptor (p75NTR), suggesting that amino acid change at G333 may affect the cell tropism of RABV [28]. Collectively, it has been clearly demonstrated that replacement of Arg_{333} or Lys_{333} to other amino acids causes a pathogenic shift of RABVs to an avirulent phenotype, while the mechanisms regulated by the amino acid residue at G333 remain unclear and controversial.

RABV infectivity of astrocytes has been reported to be dependent on the viral strain[38]. HEP-Flury–an attenuated RABV strain–shows low specificity of the cell types for *in vitro* infection[26], but shows high affinity for astrocytes *in vivo* [39]. However, involvement of the amino acid residue at G333 in astrocyte infection is yet to be established. Recently, astrocytes abortively infected with diverse neurotropic viruses, including RABV, Theiler's murine encephalomyelitis virus and vesicular stomatitis virus (VSV), have been reported to be the main source of IFN-β production in the brain conferring antiviral protection [40]. Additionally, other studies showed that type-I IFN signaling in astrocytes is important to build an antiviral state in a virus-infected brain [40–44]. RABVs are sensitive to IFN and the importance of IFN in controlling RABVs has long been proposed [45,46].

To further understand the attenuation mechanism dependent on the amino acid residue at G333 on aspects of viral infection and IFN responses in astrocytes, the tropism for astrocytes was investigated using a recombinant HEP-Flury strain (rHEP; Glu_{333}) and a single amino acid mutant $HEP^{333}R$ strain (Arg_{333}) *in vitro*. Infection of astrocytes and IFN responses

were also examined *in vivo*. Finally, the pathogenicity of rHEP was examined in mice deficient in IFN signaling pathways, which was found out to play a significant role in G333-dependent attenuation. Understanding the mechanism of RABV attenuation is essential in considering the use of live attenuated vaccines to control rabies in wild animals. Therefore, the present study has yielded new insights into the pathogenicity of RABV associated with G333.

Materials and Methods

Cell lines

Mouse neuroblastoma (NA) cells, human neuroblastoma (SYM-I) cells and baby hamster kidney cells stably expressing T7 RNA polymerase (BHK/T7-9)[47] were maintained in Eagle's Minimum Essential Medium (EMEM) supplemented with 10% fetal bovine serum (FBS). Simian virus 40 (SV40)-transformed human fetal astrocyte-derived (SVG-A) cells were propagated in Dulbecco's Modified Eagle's Medium (DMEM) supplemented with 10% FBS. SYM-I cells were cultured in type-I collagen-coated plates. All the cells above were incubated at 37°C in the presence of 5% CO_2. Expi293F cells derived from the human 293 cell line were maintained in Expi293 Expression Medium (Gibco) in spinner flasks at 37°C in the presence of 8% CO_2.

Primary cell culture

Primary cultured astrocytes were prepared from S129 mice. The whole brains from 4–5-day-old mouse pups were minced, and then incubated with papain (10 U/ml) and DNase (0.1 mg/ml) for 20 minutes. Dissociated cells were suspended in DMEM/Ham's F-12 containing 10% FBS, 100 U/ml penicillin and 0.1 mg/ml streptomycin. The cell suspension was seeded into a poly-l-lysine-coated T25 flask. After 7–8 days, the flask was shaken at 250 rpm at 37°C for at least 12 h to remove all cells except astrocytes. Adherent cells were detached with trypsin and re-seeded onto poly-l-lysine-coated 24-well plates at a density of 8.0×10^3 cells/cm^2 for virus inoculation.

Viruses

Recombinant clones of RABV (rRABV) were used in this study. The RABV HEP-Flury strain, kindly provided by Dr. Chang-Kweng Lim (National Institute of Infectious Diseases, Japan), was used as a template to generate a plasmid vector carrying the full-length cDNA of HEP strain (pHEP), as previously described[48]. The Q333R mutation was introduced into the RABV G gene by PCR-based mutagenesis and the fragment carrying the Q333R mutation was subcloned into the pHEP plasmid (pHEP^{333}R). Virus recovery was performed following a previously described procedure with some modifications[47,48]. Briefly, BHK/T7-9 cells were co-transfected with pHEP or pHEP^{333}R, and helper plasmids pT7IRES-RN, -RP and -RL. At 5 days post-transfection, the culture supernatants were passaged in NA cells for virus propagation. The infectious virus titers of rHEP and rHEP^{333}R were determined by a

focus forming assay performed as previously described[48].

Quantitative reverse transcription polymerase chain reaction (qRT-PCR)

The mRNA or viral RNA copy numbers were quantified with the Thunderbird Probe One-step qRT-PCR Kit (TOYOBO) and TaqMan probe/primer sets (Table 1) specifically targeting RABV: HEP N, mouse IFN-β, mouse Mx1, mouse oligoadenylate synthase (OAS), mouse interferon induced protein with tetratricopeptide repeats 2 (IFIT2), human IFN-β. A predesigned qPCR assay was purchased for human Mx1 (Hs.PT.58.40261042) from Integrated DNA Technologies. The expression levels of house-keeping genes were quantified using Pre-Developed TaqMan Assay Reagent Mouse ACTB or Pre-Developed TaqMan Assay Reagent Human ACTB (Applied Biosystems). The One Step TB Green PrimeScript PLUS RT-PCR Kit (Takara) was used to determine the mRNA copy number along with primer sets (Table 1) specifically targeting: mouse microtubule-associated protein 2 (MAP2), mouse ionized calcium-binding adapter molecule 1 (Iba1) and mouse glial fibrillary acidic protein (GFAP).

Recombinant human IFN-β

The cDNA fragment of human IFN-β was obtained from the transcripts of SYM-I cells infected with RABV by RT-PCR and cloned into pCXSN vector fused with a 6×-histidine tag (pCXSN-hIFN-β-his). Recombinant human IFN-β was expressed using the Expi293 Expression System (Gibco) following the manufacturer's procedure. Briefly, pCXSN-hIFN-β-his (30 μg) was transfected by ExpiFectamine 293 Reagent into Expi293F cells prepared at 3×10^6 cells/ml in 30 ml of suspension culture. Twenty hours post-transfection, the provided enhancers were added to the flask, and the cell culture supernatant was harvested at 6 days post-transfection. Recombinant human IFN-β in the supernatant was purified using Ni Sepharose Excel (Cytiva) following the manufacturer's protocols, with 400 mM imidazole for elution. The recovery and bioactivity of human IFN-β were confirmed by immunoblotting and quantification of the mRNA of the IFN-stimulated gene *in vitro*, respectively.

Quantification of IFN, and inhibition or stimulation of the IFN pathway in rRABV-infected cells

SYM-I cells cultured in collagen-coated 24-well plates were infected with rRABV at

Table 1. Primers and probes used for qRT-PCR

Target		Primer sequence (5'→3')
RABV HEP N	F[1]	GCC ACG GTT ATT GCT GCA T
	R[2]	CTC CCA AAT AGC CCC CTA GAA
	P[3]	FAM-CCC TCA TGA GAT GTC-MGB
Mouse IFN-β	F	ATG AGT GGT TGC AGG C
	R	TGA CCT TTC AAA TGC AGT AGA TTC A
	P	FAM-AAG CAT CAG AGG CGG ACT CTG GGA-TAMRA
Mouse Mx1	F	CAA TGA TCC TTT AGC TGC TAA CCT TA
	R	GTT TAC AAA GGG CTT GCT TGC T
	P	FAM-TCA GAA TGT TGC CTT TAG ACT GTG G-TAMRA
Mouse OAS	F	TGA GCG CCC ATC T
	R	CAT GAC CCA GGA CAT CAA AGG
	P	FAM-AGG AGG TGG AGT TTG ATG TGC TG-TAMRA
Mouse IFIT2	F	GGG AAA GCA GAG GAA ATC AA
	R	TGA AAG TTG CCA TAC AGA AG
	P	FAM-ATG CGT CCT TAG TCG GCT TTC TC-TAMRA
Human IFN-β	F	AAA CTC ATG AGC AGT CTG CA
	R	AGG AGA TCT TCA GTT TCG GAG G
	P	FAM-ATG GTC CAG GCA CAG TGA CTG TCC TC-BHQ1
Mouse MAP2	F	AGA CCT TCC ATC CTC CC
	R	GCC ACT TTT TCC TGC TCT GC
Mouse Iba1	F	CTT GAA GCG AAT GCT GGA GAA
	R	GCA GCT CGG AGA TAG CTT T
Mouse GFAP	F	GCT GGA GGG CGA AGA AAA CCG
	R	CAC GGA TTT GGT GTC CAG GCT GG
RABV CVS N	F	TCG AAT GCT GTC GGT CAT GT
	R	CCG AAG AAT TCC TCT CCC AAA TA
	P	FAM-CAA TCT CAT TCA CTT TGT TG-MGB

[1]Forward primer, [2]reverse primer, [3]probe

a multiplicity of infection (MOI) of 1. The expression levels of mRNA and protein of IFN-β were quantified by qRT-PCR and enzyme-linked immune sorbent assay (ELISA) using a Mouse IFN-beta ELISA Kit (R&D), respectively.

To inhibit IFN signaling, SYM-I cells were treated with anti-human IFN-receptor antibody (MAR1-5A3, Santa Cruz) at 800 ng/ml for 16 h. Then, cells were infected with rRABVs at an MOI of 0.1 and the virus titer in the cell culture supernatant was determined at 24 hours post-infection (hpi).

To stimulate IFN signaling, recombinant human IFN-β was added to the SYM-I cell culture at 600 ng/ml followed by 16 h of incubation. rRABVs were used to infect the cells at an MOI of 0.1 and culture supernatants were collected for virus titration at 48 hpi.

Animal experiments

Animal experiments were approved by the Institutional Animal Care and Use Committee of Hokkaido University (approval number 19-0014) and were performed in accordance with the committee's guidelines.

Immunocompetent S129 mice and type-I/II IFN receptor-KO AG129 mice (in a S129 background) were obtained from Marshall BioResources. S129 and AG129 mice were maintained in the Division of Molecular Pathobiology, International Institutes for Zoonosis Control, Hokkaido University.

Sex-matched 12-weeks-old S129 and AG129 mice were used for the animal studies. Mice were intracranially inoculated with 20 μl of PBS with or without 10^4 focus forming units (ffu) of rRABV under anesthesia. All mice in the survival groups were observed for 13 days for signs of symptoms and bodyweight (BW) changes. The humane endpoint was defined as a 20% decrease in BW or an inability to reach food or water because of the disease onset. For further analysis, mice were euthanized, and brain tissues were harvested at 5 days post-infection (dpi). A suspension containing 10% brain homogenate in phosphate buffered saline (PBS) was used for virus titration and RNA extraction.

Immunofluorescence assay

Cells were fixed with 10% phosphate-buffered formalin overnight and washed with PBS. Then, cells were stained by fluorescein isothiocyanate (FITC)-labelled anti-RABV N antibody (Fujirebio) together with 10 μg/ml of Hoechst 33342 for 20 min at room temperature.

Brain tissues harvested from rRABV-infected mice at 5 dpi were fixed in 10%

phosphate-buffered formalin for more than 48 h and then embedded into paraffin blocks. The paraffin blocks were sectioned at a 4-μm thickness and mounted on Platinum PRO micro glass slides (Matsunami). The sections on slides were subjected to antigen retrieval in citrate buffer for 5 min by a pressure cooker. The slides were then treated with 10% goat serum (Nichirei Biosciences) for 1 h at room temperature and incubated at 4°C overnight with primary antibodies against the following proteins: Neuronal nuclei (NeuN) (ab104224; Abcam, 1:1,000), GFAP (G9269; Sigma Aldrich, 1:400) or RABV N protein (3R7-5B12; Hytest, 1:100). After three-times washes with PBST (0.01% Tween-20 in PBS), secondary staining was performed with Alexa Fluor 488-anti-mouse IgG2a antibody (A-21131; Invitrogen, 1:1,000), Alexa Fluor Plus 594-anti-rabbit IgG (H+L) antibody (A32740; Invitrogen, 1:1,000) and Alexa Fluor 647-anti-mouse IgG2b antibody (A-21242; Invitrogen, 1:1,000) in the presence of 10 μg/ml Hoechst 33342 for 1 h at room temperature.

Microscopic analysis was conducted by LSM780 and ZEN software (Zeiss).

Isolation of astrocytes from mouse brains

Mouse brains were dissociated to cells using the Adult Brain Dissociation Kit (Miltenyi Biotec) following the manufacturer's protocol with some modifications. Briefly, a fresh whole brain was washed with cold PBS and dissected into small pieces. Aliquots were transferred into C Tubes (Miltenyi Biotec) and mixed with the provided enzymes. C Tubes were attached to the gentleMACS Dissociator (Miltenyi Biotec), and the following gentleMACS programs were performed: m_brain_01_01, m_brain_02_01, m_brain_03_01. Each program was repeated twice with 5-minute intervals on a tube rotator at 37°C. The dissociated brain was applied onto a 70 μm-cell strainer, and debris and red cell removal steps were performed in accordance with the manufacturer's protocol.

The separated cells were treated with 1% bovine serum albumin (BSA) in PBS for 30 minutes, followed by immunostaining with APC-anti-mouse ACSA2 antibody (130-116-245; Miltenyi Biotec, 1:50) and Alexa Fluor 488-anti-mouse CD11b antibody (53-0112-82; Invitrogen, 1:600) for 30 min at 4°C in the dark. After three-times washes with 0.1% BSA in PBS, cells were separated by BD FACSMelody Cell Sorter along with BD FACSChorus software (BD Biosciences).

Isolation of astrocytes was confirmed by high expression levels of the astrocyte marker (GFAP) in the sorted cells, and decreased expression levels of the neuron marker (MAP2) and microglia marker (Iba1) compared with those of the pre-sorted cells using qRT-

PCR. The data were normalized to the β-actin gene and presented as fold changes relative to the dissociated whole brain prior to the astrocyte isolation using the ΔΔCt method.

Statistical analysis

All statistical analyses were performed using GraphPad Prism software 9.2.0. For analyses between two groups, a two-tailed unpaired Student's *t*-test was used. For the comparison of two groups at multiple time points, a multiple *t*-test by the Holm–Sidak method was performed. For comparisons among more than two groups, one-way ANOVA with Tukey's multiple comparisons test was used (*p<0.05, **p<0.01, ****p<0.0001, ns=not significantly different). Data were presented as the mean ± standard deviation (SD) in graphs.

Results

Impact of amino acid substitution at position 333 of the G protein on rRABV growth in neuron- and astrocyte-derived cell lines

To investigate the role of G333 on RABV infection, rRABV clones, *i.e.* rHEP carrying Glu_{333} and rHEP^{333}R carrying Arg_{333} in G protein, were generated by the reverse genetics method. First, the replication efficacy was evaluated between rHEP and rHEP^{333}R in a neuron-derived cell line, NA cells, and an astrocyte-derived cell line, SVG-A cells. rHEP and rHEP^{333}R showed similar growth kinetics in NA cells (Fig. 1A). By contrast, in SVG-A cells, rHEP exhibited a significantly higher infectious virus titer at 24- and 48- hpi compared with rHEP^{333}R. No growth of rHEP^{333}R was observed in SVG-A cells (Fig. 1A). These results were reflected in the population of infected cells stained by FITC-labeled anti-RABV N antibody. In short, rHEP and rHEP^{333}R exhibited similar infectivity to neuron-derived NA cells, whereas rHEP^{333}R showed limited growth in astrocyte-derived SVG-A cells (Fig. 1B). These results demonstrated that the amino acid residue at G333 influences the cell tropism of RABV.

IFN production in primary astrocytes infected with rRABVs

Astrocytes act as IFN producers in brain tissue infected with neurotropic viruses [40–44], and thus, the relationship between RABV infection and IFN responses in astrocytes was assessed. Primary astrocytes were used in these experiments because the astrocyte-derived cell line SVG-A lacks an IFN responses against rRABV infection (Fig. 2A). In line with the results of rRABV growth in SVG-A cells (Fig. 1), mouse-derived primary astrocytes were susceptible to rHEP infection but less susceptible to rHEP^{333}R infection (Fig. 2B). To confirm whether rRABV infection triggers IFN production in astrocytes, the mRNA levels of IFN-β in rRABV-infected primary astrocytes were quantified by qRT-PCR. The *IFN-β* gene expression levels in primary astrocytes were significantly higher in rHEP-infected cells than that in rHEP^{333}R -infected cells (Fig. 2C). These results suggested that rHEP can more efficiently infect astrocytes and induce subsequent IFN production compared to rHEP^{333}R.

rRABV tropism for astrocytes and the IFN responses in vivo

To further characterize the role of an amino acid at G333 with respect to astrocyte infection and IFN induction, astrocytes were isolated from the brains of immunocompetent S129 mice at 5 days after intracranial inoculation of rHEP or rHEP^{333}R (Fig. 3A and 3B).The

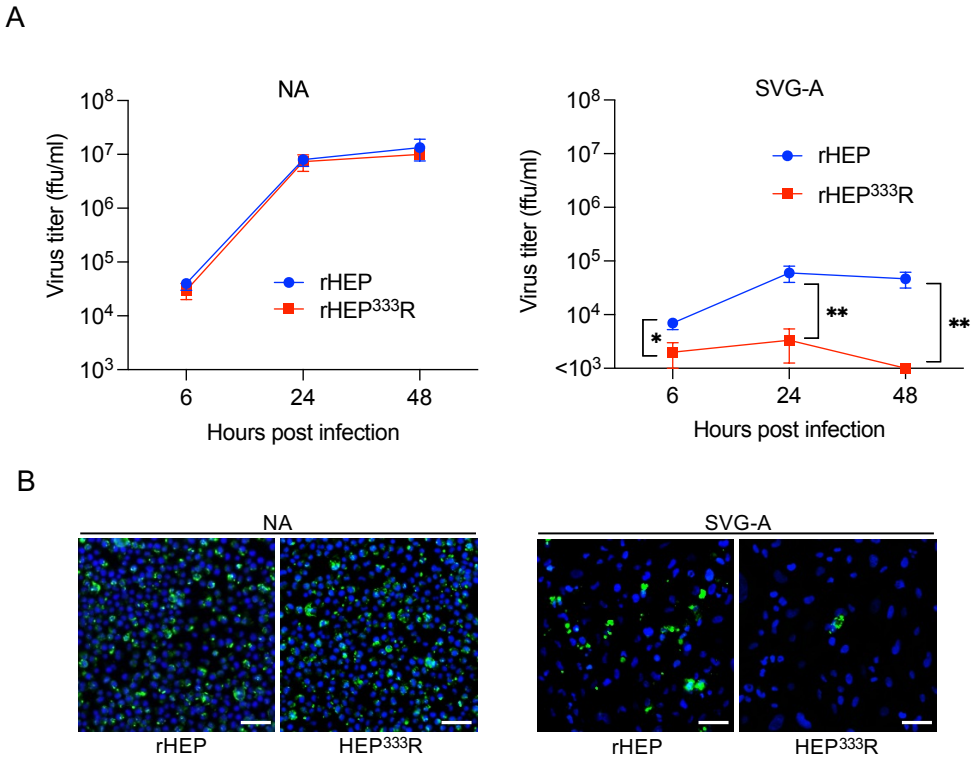

Figure 1. Infectivity of RABV in neuron-derived NA cells and astrocyte-derived SVG-A cells

Monolayers of NA or SVG-A cells were inoculated with rHEP or rHEP^{333}R at MOI of 1. (A) Viral growth curve. Supernatants were collected at the indicated time points and virus titers were measured by a focus forming assay. Means ± SD of triplicate data from a representative experiment are shown in the graph. A multiple *t*-test was performed by the Holm–Sidak method for statistical analysis. *p<0.05, **p<0.01. (B) Images of RABV-infected cells. Cells were fixed at 24 hpi and stained with FITC-conjugated anti-RABV N antibody for RABV N (green) and Hoechst 33342 for the nucleus (blue). The representative images were captured by fluorescent microscopic analysis. Scale bar; 50 μm.

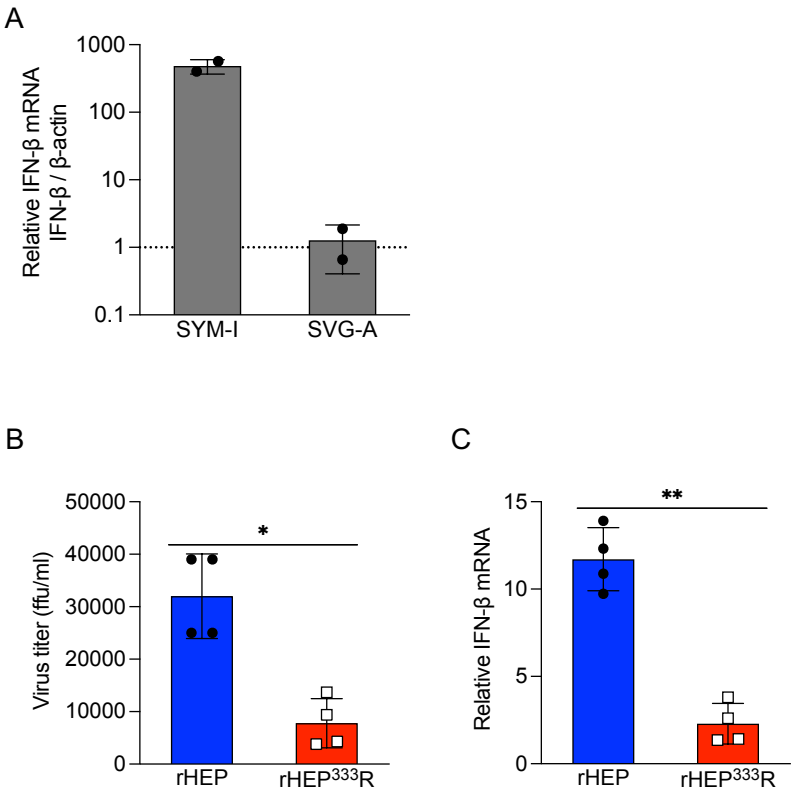

Figure 2. Infectivity of RABV in mouse-derived primary astrocytes

(A) Expression of IFN-β mRNA of neuron-derived SYM-I cells and astrocyte-derived SVG-A cells in response to RABV infection. SYM-I cell and SVG-A cell in a monolayer were inoculated with rHEP at an MOI of 1. IFN-β gene expression level quantified by qRT-PCR at 24 hpi. The data were normalized to the β-actin gene and presented as fold changes relative to the mock controls using the ΔΔCt method. The graphs show the means ± SD of duplicate data. (B), (C) Astrocyte-derived primary cells were cultured on 24-well plates to 80% confluency and infected with rHEP or rHEP^{333}R at an MOI of 1. Supernatants and RNAs were collected at 48 hpi and subjected to virus titration by a focus forming assay (A) and qRT-PCR for the measurement of IFN-β gene expression (B), respectively. Expression levels of the IFN-β gene were normalized to the β-actin gene and presented as fold changes relative to the mock controls using the ΔΔCt method. The values in the graph show the means ± SD of a representative experiment. Statistical analysis was performed by the Student's *t*-test (*p<0.05, **p<0.01).

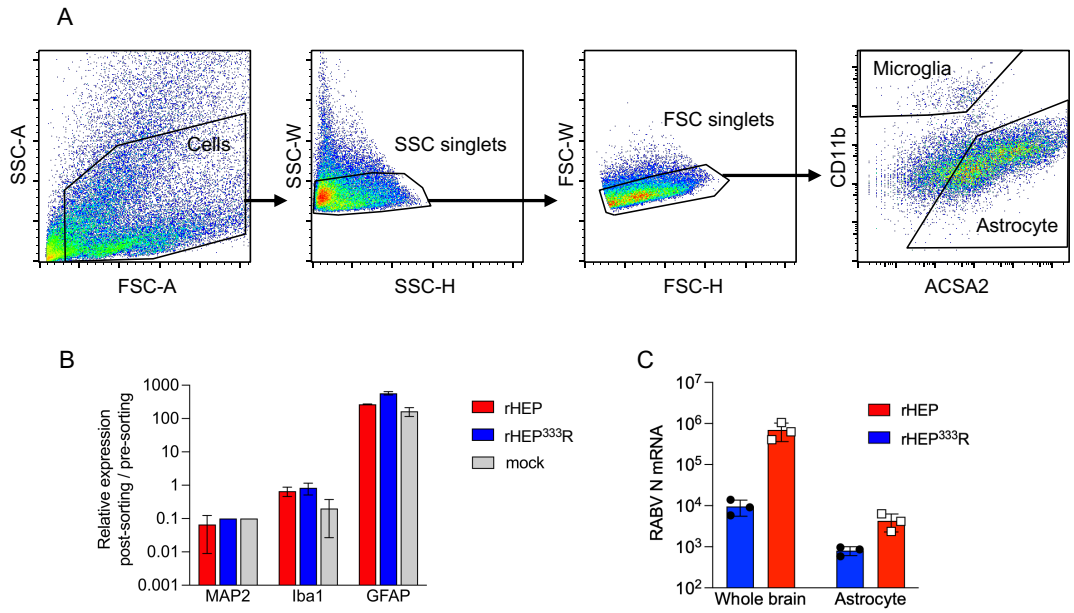

Figure 3. Infectivity of RABV and IFN expression in astrocytes in the brains of mice infected with rRABVs

(A) Gating strategy of astrocytes from mouse brains. Mouse brains were dissociated with the Adult Brain Dissociation Kit (Miltenyi Biotec) and dissociated cells were labeled with antibodies against CD11b for microglia and astrocyte cell surface antigen-2 (ACSA2) for astrocytes. Cell populations were gated as singlets based on the profiles of side scatter (SSC) and forward scatter (FSC). According to the cytogram of CD11b and ACSA2, ACSA2-positive astrocytes were sorted by the FACSMelody Cell Sorter along with FACSChorus software (BD Biosciences). Images were visualized by FlowJo (BD Biosciences). (B) Isolation of astrocytes from mouse brains was confirmed by examination of the mRNA expression of cell markers: MAP2 for neurons, Iba1 for microglia and GFAP for astrocytes. The data were normalized to the β-actin gene and presented as fold changes relative to the dissociated whole brain prior to the astrocyte isolation using the ΔΔCt method. High expression levels of the astrocyte marker (GFAP) were observed for the sorted cells, whereas the expression levels of the neuron marker (MAP2) and microglia marker (Iba1) were decreased compared with those of the pre-sorted cells. (Continued on next page)

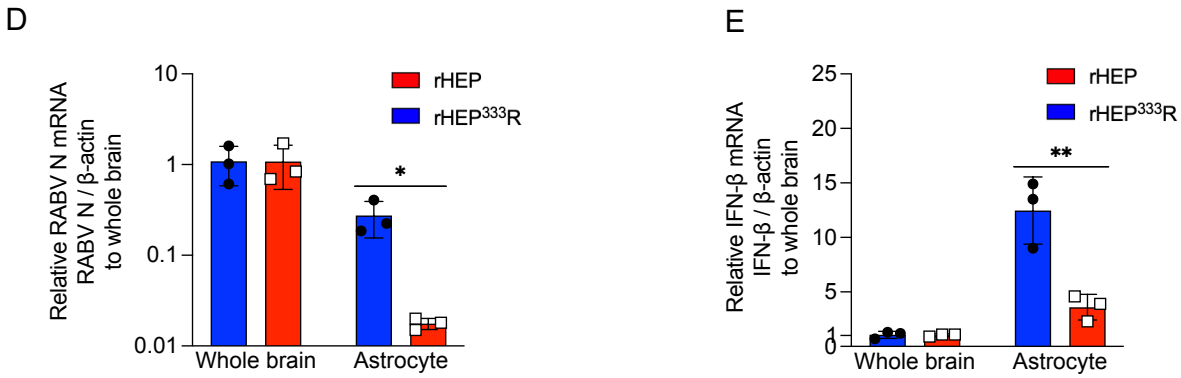

Figure 3. (Continued)

(C–E) S129 mice were inoculated intracranially with 10^4 ffu of rHEP or rHEP^{333}R. qRT-PCR was performed using homogenate of the brain tissue and isolated astrocytes at 5 dpi. I RABV N mRNA copy numbers. The data were quantified by the standard curve method and normalized to the β-actin gene expression. (D) Relative RABV N mRNA level in astrocytes. The data were normalized to the β-actin gene and presented as fold changes relative to the whole brain using the ΔΔCt method. (E) Relative IFN-β mRNA expression in astrocytes. The data were normalized to the β-actin gene and presented as fold changes relative to the whole brain using the ΔΔCt method. All values in the bar graph show the means ± SD of three mice from a representative experiment. Statistical analysis was performed by the Student's *t*-test (*p<0.05, **p<0.01).

viral RNA replication was detected in both whole brain and isolated astrocytes (Fig. 3C). To estimate the incidence of rRABV infection in astrocytes in the whole brain, viral RNA levels were quantified in astrocytes sorted from the rRABV-infected brain and the data were described relative to viral replication in the whole brain (Fig. 3D). In rHEP-infected mice, viral RNA levels in astrocytes relative to the whole brain were significantly higher than these in rHEP^{333}R-infected mice (Fig. 3D), suggesting preferential infection of astrocytes by rHEP *in vivo*. Similarly, and consistent with the viral RNA levels, the gene expression levels of IFN-β were higher in astrocytes derived from rHEP-infected mice compared with those from rHEP^{333}R-infected mice (Fig. 3E). These results indicated that rHEP has tropism for astrocytes and induces high levels of IFN production in astrocytes *in vivo*.

Comparison of infectivity and pathogenicity between rHEP and rHEP^{333}R in IFN-receptor knockout (KO) mice

rHEP is an attenuated RABV strain that causes transient infection in immunocompetent mice [26]. To evaluate the protective efficacy of IFN in mice infected with rHEP, next the pathogenicity of rRABV was examined in AG129 mice; type-I/II IFN receptor-knockout (KO) mice in a S129 background, which are highly susceptible to infection by various viruses [49–51]. AG129 and S129 mice were infected with rRABVs intracranially to evaluate virus replication and host IFN responses in the central nervous system. Consistent with a previous report [26], rHEP caused a transient decrease in BW without any neurological symptoms in immunocompetent S129 mice (Fig. 4A); however, rHEP^{333}R showed BW loss and neuropathogenicity at 6 dpi, resulting in 100% mortality by 8 dpi (Fig. 4B). In contrast, in AG129 mice, rHEP as well as rHEP^{333}R caused significant body weight loss and fatal neurological manifestations at 4–5 dpi, resulting in a 100% fatality rate at 6 dpi (Fig. 4A and 4B). Furthermore, virus titration of the whole brain tissue at 5 dpi showed a high virus titer in S129 mice infected with rHEP^{333}R compared with rHEP (Fig. 4C). Conversely, there was no remarkable difference in virus titer in AG129 mice infected with rHEP or rHEP^{333}R (Fig. 4C). The virus titers in AG129 mice infected with rHEP and rHEP^{333}R were approximately 10^4 or 10^2 times higher than in S129 mice infected with rHEP and rHEP^{333}R, respectively (Fig. 4C). These results indicated that attenuated rHEP exhibits similar growth and virulence to the authentic pathogenic RABV in AG129 mice, intimating that the IFN responses may be related to the attenuation of rHEP in immunocompetent mice. Consistent with the observations on virus titration (Fig. 4C), no significant difference in IFN gene expression

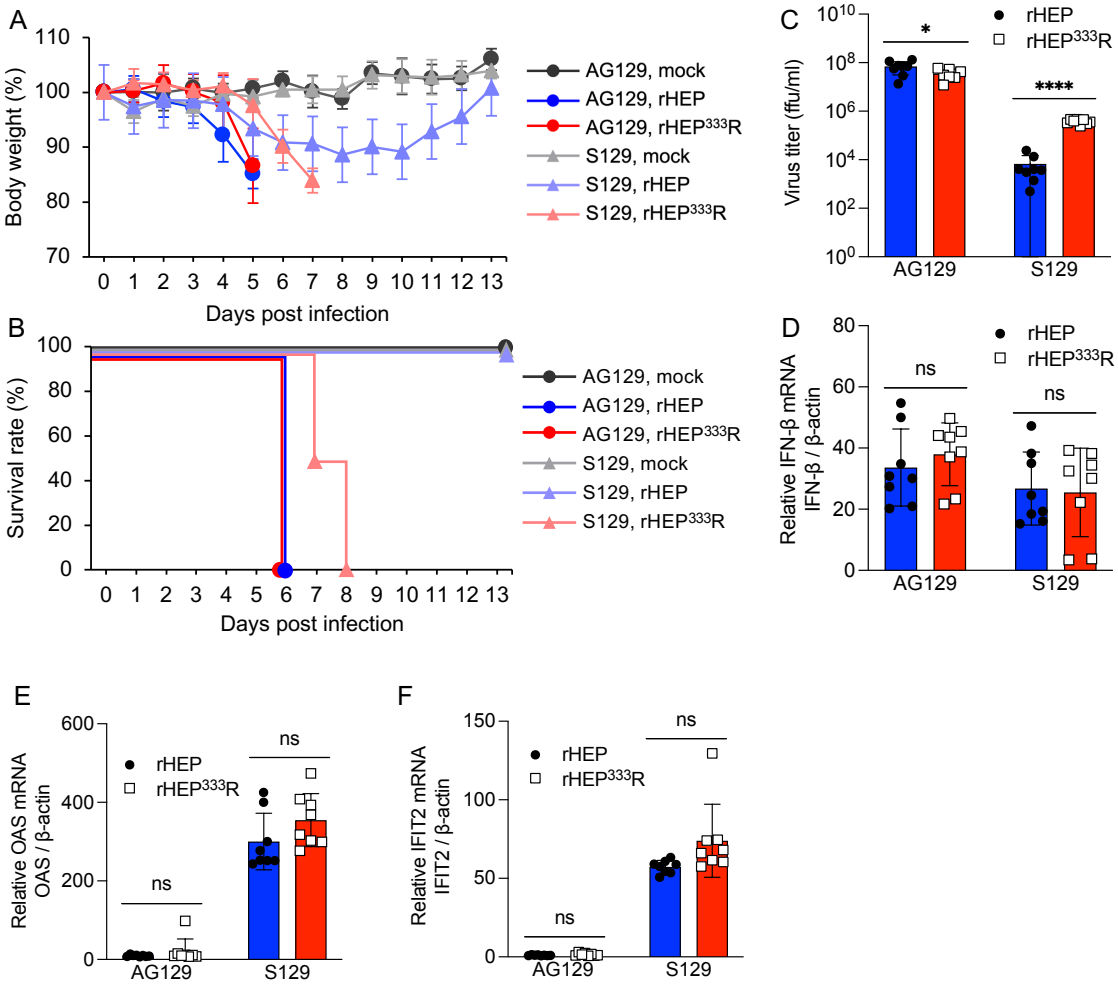

Figure 4. Evaluation of RABV pathogenicity in IFN-receptor knockout mice

Twelve-week-old AG129 or S129 mice were intracranially inoculated with 10^4 ffu of rHEP or rHEP^{333}R. Virus-infected mice were monitored for (A) body weight changes and (B) survival every day until 13 dpi. The values in the graph are shown as the means ± SD (mock group; n=4, virus challenge group; n=8). (C) Virus titer in the 10% homogenate of the whole brain at 5 dpi was determined by a focus forming assay. The bar graphs show the means ± SD (n=8). (D–F) mRNA expression of IFN-β, OAS or IFIT2 in the mouse brains at 5 dpi was determined by qRT-PCR. The results were normalized to the β-actin gene and presented as fold changes relative to the mock controls using the ΔΔCt method. The bar graphs show the means ± SD (n=8). Statistical analysis was performed by the Student's *t*-test (*p<0.05, ****p<0.0001).

levels was found between the two viruses in AG129 mice (Fig. 4D). Interestingly, no significant difference was observed in expression levels of IFN-β gene or IFN-stimulated genes (ISGs) in S129 mice infected with rHEP or rHEP^{333}R (Fig. 4D–F), despite the virus titer being markedly higher in rHEP^{333}R-infected S129 mice (Fig. 4C). Considering the relatively low virus titer and high IFN gene expression level of rHEP in S129 mice, rHEP may have induced IFN-β gene or ISGs expression more strongly than rHEP^{333}R in S129 mice.

Immunofluorescence assay of brain sections from rRABV-infected mice showed extensive viral infection in the neurons of AG129 mice infected with either rHEP or rHEP^{333}R (Fig. 5A). Notably, rHEP effectively infected astrocytes as well as neurons in AG129 mice compared with rHEP^{333}R (Fig. 5B, 5E, and 5F). In S129 mice infected with rHEP, a limited number of neurons and astrocytes were found to be positive for RABV N proteins (Fig. 5C and 5D). Even though rHEP^{333}R showed RABV signals distributed across the whole brain in S129 mice, RABV-infected astrocytes were rarely observed in S129 mice (Fig. 5D). These results strengthen the hypothesis that astrocytes are highly susceptible to infection with rHEP but not rHEP^{333}R *in vivo*.

IFN induction and the sensitivity of rRABVs in neuronal cells

Finally, to further investigate the relationship between the IFN responses and pathogenicity of the rRABVs, IFN inducibility and the sensitivity of rRABVs under an IFN-mediated antiviral state was compared using a human neuroblastoma cell line SYM-I, in which IFN signaling pathways are validated [52]. SYM-I cells were appropriate to evaluate the ability of IFN induction and the sensitivity of rRABVs because the growth kinetics of rRABVs were comparable in this cell line (Fig. 6A). Then IFN-β responses against rRABV infection was analyzed and it was found that IFN-β production was consistent between the two rRABVs both at the mRNA (Fig. 6B) and the protein level (Fig. 6C) in culture supernatants. These results indicated that there is no difference between rHEP and rHEP^{333}R in terms of IFN-β inducibility in response to virus infection.

Next, the sensitivity of rRABVs to the antiviral state induced by IFN was examined. An appropriate dose of IFN-β pretreatment was determined by a response of Mx1 to induce antiviral state in SYM-I cells (Fig. 6D). Under the antiviral conditions, the proliferations of both rHEP and rHEP^{333}R were inhibited in SYM-I cells (Fig. 6E). By contrast, when the IFN signaling pathway was blocked by treatment of the cells with anti-IFN receptor neutralizing

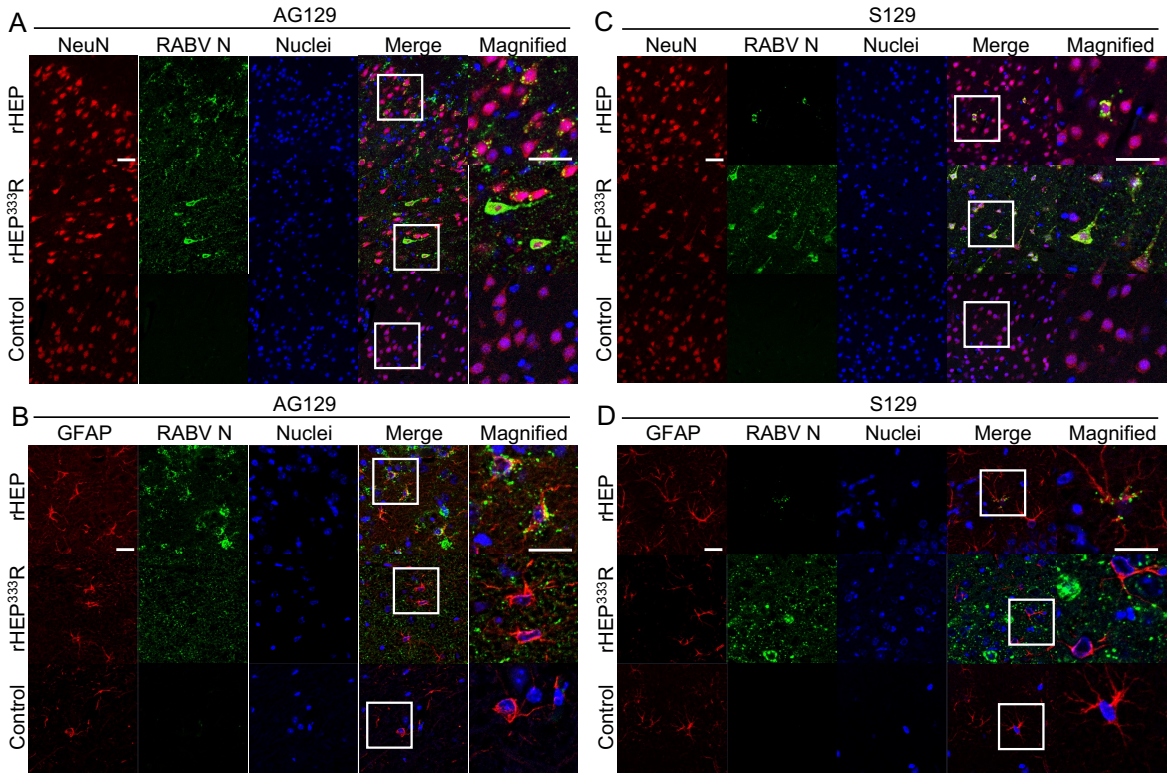

E

	Cerebral cortex			Hippocampus		
	Counted cell number	RABV positive %	SD	Counted cell number	RABV positive %	SD
rHEP	93	69.04	5.02	149	76.23	10.75
rHEP^{333}R	92	29.31	12.29	121	32.05	15.44

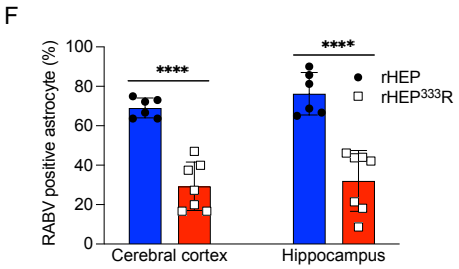

Figure 5. RABV tropism in mouse brain

Twelve-week-old AG129 or S129 mice were intracranially inoculated with 10^4 ffu of rHEP or rHEP^{333}R. (A–D) Brain sections of AG129 and S129 mice at 5 dpi were stained for (A, C) NeuN or (B, D) GFAP, and RABV N protein. Scale bar; 20 μm. (E) Summary of counting RABV-positive astrocytes in cerebral cortex and hippocampus of AG129 mice. (F) RABV-positive rate of astrocytes in AG129 mice. The number of RABV N-positive astrocytes were manually counted in 3 snapshots of cerebral cortex and hippocampus per section. Two animals were analyzed for each virus. Each dot represents positive rate of each snapshot. The bar graphs show the means ± SD. Statistical analysis was performed by the Student's *t*-test (***p<0.0001).

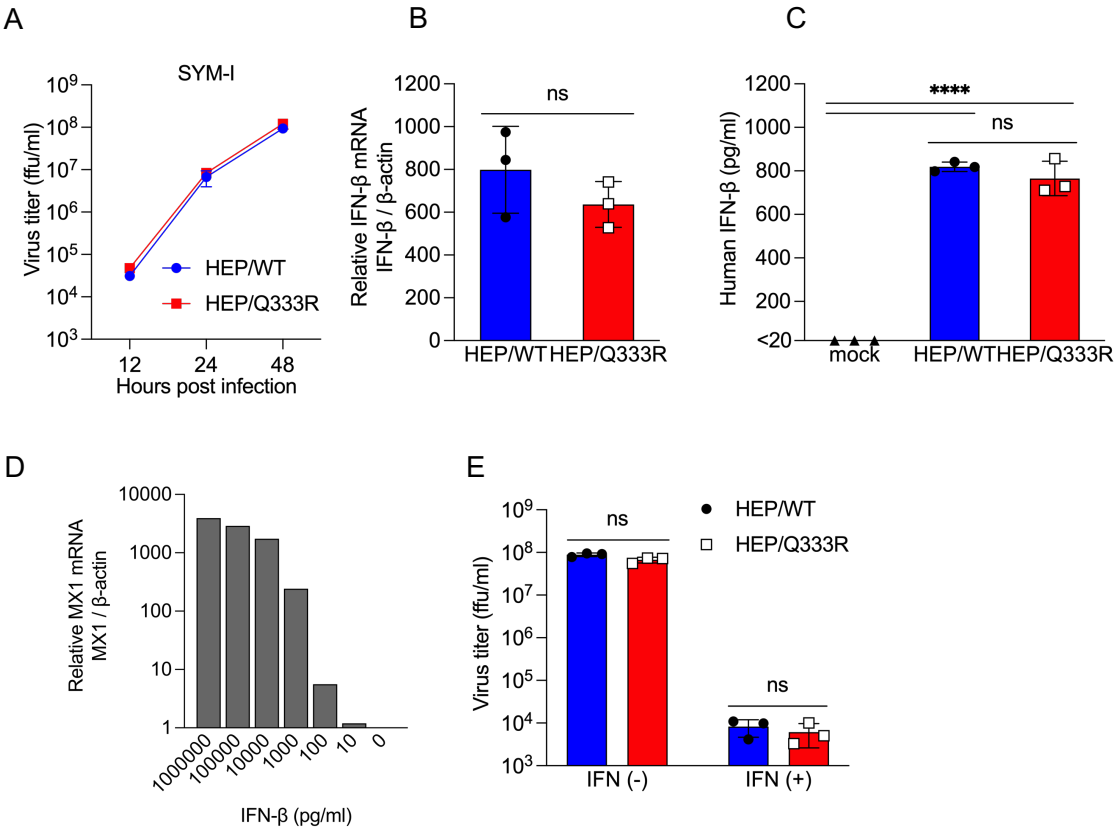

Figure 6. Susceptibility and resistance of RABV to IFN *in vitro*

Human neuron-derived SYM-I cells were used for this series of experiments. (A–C) SYM-I cells in a monolayer were inoculated with rHEP or rHEP^{333}R at an MOI of 1. (A) Viral growth curve. Virus replication at the indicated time points was evaluated by qRT-PCR using the standard curve method. (B) IFN-β gene expression level quantified by qRT-PCR at 48 hpi. (C) IFN-β protein level in culture supernatants was measured by ELISA at 48 hpi. (D) Stimulation of IFN signaling by treatment with recombinant IFN-β. Cells were treated with exogenous human IFN-β at the indicated concentration for 16 h at 37°C. Thereafter, RNA was extracted from the cells and subjected to qRT-PCR of the Mx1 gene, an IFN-stimulated gene. (E) Stimulation IFN pathways by treatment with recombinant IFN-β. Cells were treated with exogenous human IFN-β at 600 ng/ml in culture medium for 16 h prior to RABV infection at an MOI of 0.1. Virus titers in the supernatants at 48 hpi was measured by a focus forming assay. (Continued on next page)

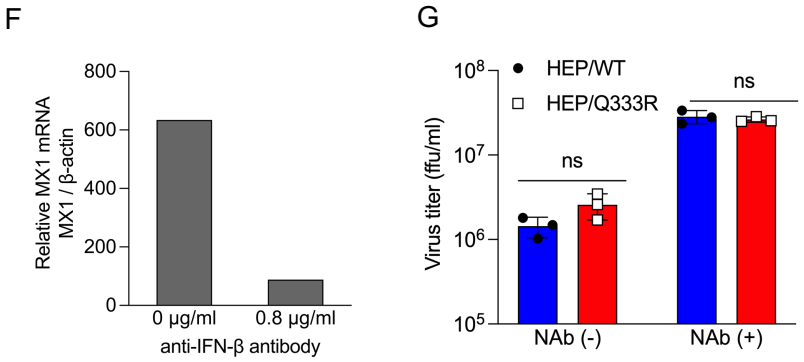

Figure 6. (Continued)

(F), (G) Neutralization of IFN signaling. Cells were treated with anti-human IFN receptor neutralizing antibody at 800 ng/ml in the culture medium for 16 h prior to rRABV infection at an MOI of 0.1. RNA was extracted at 24 hpi and subjected to qRT-PCR of the Mx1 gene (F). The data were normalized to the β-actin gene and presented as fold changes relative to the controls without the antibody using the ΔΔCt method. (G) Virus titer in the supernatant at 24 hpi was measured by a focus forming assay. Results of qRT-PCR were normalized to the β-actin gene and presented as fold changes relative to the mock controls using the ΔΔCt method. Values in the graphs show the means ± SD of triplicate data from a representative experiment. Statistical analysis was performed by multiple *t*-tests using the Holm–Sidak method for (A), Student's *t*-test for (B), (E) and (G), and standard one-way ANOVA and Tukey's multiple comparisons test for (C) (****$p<0.0001$, ns=not significant).

antibody (Fig.6F), the progeny virus titer was increased at the same rate for rHEP and rHEP^{333}R relative to the control infection (Fig. 6G). These results suggested that rHEP and rHEP^{333}R have similar potential to induce IFN and similar sensitivity to the subsequent antiviral state induced by IFN.

Discussion

RABV G plays major roles in RABV pathogenicity in terms of cell attachment, apoptosis induction and stimulation of the host immune responses [22,30,37,53–55]. In particular, an amino acid residue at position 333 in the G protein (G333) has been shown to be a major determinant of RABV pathogenicity and attenuation [36,56]. To further understand the mechanism underlying the attenuation of RABV dependent on the amino acid residue at G333, this study focused on RABV tropism specifically for astrocytes using a RABV non-pathogenic strain (rHEP) carrying Glu_{333} and a pathogenic mutant (rHEP^{333}R) carrying Arg_{333} in G protein. Herein, it was demonstrated that astrocytes are susceptible to infection with rHEP but not rHEP^{333}R both *in vitro* and *in vivo*. These results indicated that the infectivity of the attenuated strain HEP in astrocytes is dependent on a single amino acid at G333 and that Glu_{333} has a higher affinity for astrocytes than Arg_{333}.

Previous studies have reported that avirulent RABV strains including rHEP carrying Glu_{333} in RABV G exhibit a broader cell tropism not specific to neuronal cells [25,26] compared to pathogenic strains carrying Arg_{333} or Lys_{333}. Findings in this chapter indicated that replacement of Arg_{333} to Glu_{333} increased astrocyte tropism of HEP strain. Even though the position G333 is not located at any of reported receptor binding sites on the RABV G [57–59], replacement of Arg_{333} with Glu_{333} is known to greatly reduce the binding affinity of RABV G to one of the RABV receptors, p75NTR [28]. Accordingly, the amino acid residue at G333 might influence the conformation of the receptor binding sites of RABV G, possibly altering the RABV tropism for astrocytes.

In cells, virus infection induces IFN-β production immediately, and mass production of IFN-α/β is triggered by the earlier IFN-β response[60,61]. Previously, abortive virus infection in astrocytes was found to be the main source of IFN production in the central nervous system [40]. Besides, RABV infection of astrocytes has been reported to be abortive[40,41]. In this study, the viral RNA replications were detected in isolated astrocytes from RABV-infected S129 mice (Fig. 3C) in contrast to RABV N protein signals rarely found in astrocytes in S129 mice (Fig. 5D) compared with AG129 mice (Fig. 5B). Based on these observations, infection of astrocytes in immunocompetent mice may be abortive with IFN responses activated as previously reported [40,41]. Additionally, compared to rHEP, rHEP^{333}R showed lower infectivity to astrocytes (Fig. 1–3, 5B, 5E, and 5F) and consequently induced lower IFN-β production in astrocytes (Fig. 2C and 3D) which were not due to their IFN inducibility or susceptibility to IFN (Fig. 6B, 6C, and 6E). Finally, in the absence of an IFN response, rHEP showed an

equivalent level of virus replication and pathogenicity to rHEP^{333}R both *in vitro* (Fig. 6G) and *in vivo* (Fig. 4A–C). These results suggested that IFN production in astrocytes is associated with attenuation of rHEP.

Previous studies have proposed several possible mechanisms of G333-dependent RABV attenuation. HEP strain comprising Glu_{333} in RABV G has been reported to induce higher levels of apoptosis in infected neurons than pathogenic RABVs carrying Arg_{333} or Lys_{333} [25,37]. However, another attenuated Evelyn-Rokitnicki-Abelseth (ERA) strain carries the Arg_{333} but also caused apoptosis[22]. In addition, it has been also demonstrated the poor neuronal transmissibility of HEP strain *in vivo*, which is one of the attenuation properties, was gained by the substitution of Glu_{333} to Arg_{333} in RABV G. Conversely, high pathogenic CVS strain lost its virulence by mutation at Arg_{333} without changing its distribution pattern in brain[62] or neuroinvasiveness which was lost by an additional mutation at Lys_{330} in RABV G [63]. These previous findings suggest that the amino acid residue on G333 could contribute to the attenuation of RABV in multiple aspects, which is dependent on the specific RABV strains. The new mechanism, claimed here, of Glu_{333}-dependent astrocyte infection and IFN responses at least partially could contribute to the attenuation of HEP strain. In fact, ERA strain comprises Arg_{333} in the RABV G and showed less infection of astrocytes[38], which fits to the G333-dependent astrocyte infection claimed here. Besides, it may be possible that avoiding the astrocyte-related host immunity responses by carrying Arg_{333} (or Lys_{333}) in RABV G is one of the strategies for the efficient replication of some pathogenic RABV strains. However, recent studies have shown that other field RABV strains or even some bat-associated lyssaviruses could cause infection in astrocytes regardless of the amino acid at G333 or pathogenicity[38,64]. Based on these previous findings, it should be noted that the amino acid residue at position 333 alone is not sufficient to determine astrocyte tropism. In this chapter, it is considered that rHEP was cleared by the IFN-mediated anti-viral responses in astrocytes leading to its attenuation. However, even if virus could infect to astrocytes and induce IFN responses in astrocytes, whether the virus could overcome the anti-viral states should be dependent on its anti-IFN capacity or even other factors. Therefore, RABV attenuation due to G333-dependent astrocyte infection and IFN responses is not always applicable for general RABV or lyssaviruses but for the specific strains or conditions.

In conclusion, the present study have demonstrated here that rHEP more efficiently and more frequently infected astrocytes than rHEP^{333}R and, consequently, evoked higher IFN responses in astrocytes *in vitro* and *in vivo*. In addition, it was revealed that the IFN response

is indispensable for both virulence and attenuation of rHEP using AG129 mice deficient in IFN responses. Taken together, these findings confirm that Glu_{333} in RABV G is involved in the attenuation of rHEP, at least partially, by excessive infection of astrocytes triggering the induction of IFN. It provides new insights into the mechanism of RABV virulence attenuation and highlights the importance of astrocytes as potential drivers of the host immune response against lethal infection with RABV. In future studies, a profound understanding of RABV infection of astrocytes and the evoked immune responses should help to unravel the mechanism of RABV attenuation and clearance.

Chapter II:

Morphogenesis of bullet-shaped rabies virus particles requires a functional interplay between the viral matrix protein and ESCRT-I component TSG101

Summary

Viral protein assembly and virion budding are tightly regulated to enable the proper formation of progeny virions. At this late stage in the virus life cycle, some enveloped viruses take advantage of the host endosomal sorting complex required for transport (ESCRT) machinery, which contributes to the physiological functions of membrane modulation and abscission. Bullet-shaped viral particles are unique morphological characteristics of rhabdoviruses; however, the involvement of host factors in rhabdovirus infection, and specifically the molecular mechanisms underlying virion formation are poorly understood. In the present study, a siRNA screening approach was used to find out that the ESCRT-I component TSG101 contributes to the propagation of RABV. The data demonstrated that the RABV M interacts with TSG101 *via* the late-domain containing the PY and YL motifs, which are conserved in various viral proteins. Loss of the YL motif in the RABV M or the downregulation of host TSG101 expression resulted in the intracellular aggregation of viral proteins and abnormal virus particle formation, indicating a defect in the RABV assembly and budding processes. These results indicate that the interaction of the RABV M and TSG101 is pivotal for not only the efficient budding of progeny RABV from infected cells but also for the bullet-shaped virion morphology.

Introduction

During the RABV virion assembly stage, the viral RNA genome is surrounded by RABV N together with P and L to form RNP in a firmly organized helical structure. The assembly of the RNP continues with an interaction with the RABV M, which provides a "skeleton structure," and the RNP is finally enveloped by the cellular lipid bilayer containing the RABV G[20]. The M-condensing RNP structure is essential for the bullet-shaped viral particles that are a characteristic feature of rhabdoviruses.

In terms of budding and viral particle formation, the importance of the RABV M and G has been highlighted. The RABV G forms membrane microdomains, creates bud sites, and pulls viral particles[65]. RABV M makes a major contribution to the pushing out and pinching off virions as well as promoting efficient virus budding and particle formation, and it binds to RNPs to enable their assembly beneath the cell membrane[20,66–69]. Although G-deficient RABV forms noninfectious but bullet-shaped particles, M-deficient RABV rarely forms infectious virus and produces filamentous particles[20,70]. Therefore, RABV M is an essential component in the formation of the bullet-shaped particle structure of RABV.

Some enveloped viruses hijack cellular factors including the ESCRT machinery, to facilitate the budding process. ESCRTs build complexes by sequentially recruiting ESCRT-0, -I, -II, and -III factors during membrane trafficking, e.g., in the multivesicular body sorting pathway[71–73]. The general physiological roles of ESCRTs include the deformation and abscission of lipid membranes, which occur *via* a process similar to that of virus budding[71,72]. Viral proteins carry consensus amino acid sequences, such as the PY, YL, and PTS/AP motifs, which are called late (L)-domains because they play a role in the recruitment of ESCRT factors at the late stages of the viral life cycle. For example, the human immunodeficiency virus Gag protein and the Marburg virus and Ebola virus VP40 interact with ESCRT-related proteins, such as Alix and TSG101, *via* their L-domain to promote budding[74–76]. However, little is known about the involvement of ESCRTs in rhabdovirus infection, including RABV infection. Recent proteomic profiling has revealed that ESCRT-related factors, such as chmp4B, HSP40, Alix, TSG101, and chmp2A, are present in purified RABV virions[77]. In addition, RABV M possesses L-domains consisting of the PY and YL motifs, and a previous study revealed that mutations in the PY motif of RABV M led to both the reduced budding efficiency and pathogenicity of RABV in mice[78]. However, the molecular mechanisms underlying the ESCRT-mediated virion assembly and budding in RABV-infected cells has not been clarified.

In this chapter, TSG101, a member of the ESCRT-I proteins, was identified as a binding partner of RABV M during the late stage of the virus life cycle. Both the PY and YL motifs of RABV M act as a functional L-domain to enable the interaction with TSG101. RABV propagated in the absence of TSG101 or a recombinant RABV mutant lacking the YL motif failed to bud from the cell membrane and instead formed disrupted virions. Overall, these findings indicate that TSG101 and the L-domain of RABV M are responsible for efficient virus budding and the bullet-shaped morphology of RABV.

Materials and Methods

Cells

Human neuroblastoma (SK-N-SH) cells, mouse neuroblastoma (NA) cells, and baby hamster kidney cells stably expressing T7 RNA polymerase (BHK/T7-9) cells[47] were maintained in EMEM supplemented with 10% FBS. SK-N-SH cells were cultured in type-I collagen–coated plates, whereas 293T cells were cultured in DMEM supplemented with 10% FBS. All cells were incubated at 37°C in the presence of 5% CO_2.

SK-N-SH cells stably expressing TSG101–venus were established using lentivirus transduction. cDNA fragments encoding TSG101 fused at its N-terminus with venus following double GGGGS linker sequences were subcloned into the pLVSIN-CMV Pur vector. The resulting plasmid was transfected into 293T cells using Lentiviral High Titer Packaging Mix (Takara) to obtain the lentiviral vector for TSG101–venus transduction. The SK-N-SH cells were then infected with the lentivirus vector and selected using puromycin.

Viruses

Recombinant RABV clones of the CVS strain, HEP strain, and a reporter CVS encoding NanoLuc [CVS-Nluc (N-P)] were prepared as described previously[48,79]. Recombinant RABV/PY and RABV/YL mutants were obtained from the cDNA clones of the CVS strain by substituting the PY and YL motif for alanine, respectively, which was achieved *via* PCR-based mutagenesis according to procedures described previously[47,48,79]. The street RABV Toyohashi strain was prepared as described previously[7]. All viruses were propagated in NA cells.

qRT-PCR

Viral RNA copy numbers were quantified using a Thunderbird Probe One-step qRT-PCR Kit (TOYOBO) and TaqMan probe/primer sets specifically targeting RABV CVS N (Table 1).

RNAi screen

A custom siRNA library targeting 25 ESCRT-related factors and consisting of three different siRNAs per target gene was used to rule out the off-target effect (Silencer Select predesigned siRNA, Ambion). SK-N-SH cells were reverse-transfected with 20 nM of siRNA using Lipofectamine RNAiMAX (Invitrogen) in collagen-coated 96-well plates and then

cultured for 60 h. Subsequently, the cells were infected with CVS-Nluc (N-P) at a MOI of 10. At 18 hpi, the supernatants were transferred into NA cells seeded on 96-well clear-bottom black plates. After 8 h of incubation at 37℃, luminescence signals were measured using a Nano-Glo Luciferase Assay (Promega) following the manufacturer's protocol.

Virus titration via a focus forming assay

NA cells were infected with serially diluted specimens in a 48-well plate for 1 h and then overlayed with MEM supplemented with 5% FBS, 0.5% methyl cellulose, and GlutaMAX (Gibco). After 3 days of incubation, the cells were fixed and stained with FITC-labelled anti-RABV N antibody (Fujirebio) as well as 10 μg/ml of Hoechst 33342. Foci were then counted to determine the virus titer in ffu.

Antiviral activity of ilaprazole, a TSG101 inhibitor

Cells were infected with viruses at a MOI of 1 in the presence of ilaprazole (SelleckChem) serially diluted in 5% FBS-supplemented MEM for 1 h. After the cells were washed with PBS, fresh medium containing ilaprazole was added. Progeny viruses in the supernatants were titrated at 24 hpi.

Rescue experiment

SK-N-SH cells were first transfected with 20 nM of siRNA against TSG101 using Lipofectamine RNAiMAX (Invitrogen). At 48 h post-transfection of siRNA, the cells were transfected with siRNA-resistant TSG101 constructs using Lipofectamine 2000 (Invitrogen). After 24 h of incubation, the cells were infected with CVS at a MOI of 1, and the supernatant was collected for virus titration at 24 hpi.

Attachment and entry assay

The attachment and entry assays were conducted following procedures described previously[80]. Briefly, for the attachment assay, SK-N-SH cells were infected with RABV at MOI of 10 at 4℃ for 1h and washed with PBS followed by RNA extraction. For the entry assay, cells were infected with RABV at MOI of 10 at 37℃ for 30 min and washed with PBS followed by trypsinization and RNA extraction. The cell-attached virions and internalized virions were analyzed by measuring viral genome copies using qRT-PCR.

Minigenome assay

A CVS strain-based minigenome assay was performed according to a previously reported method with some modification[81] and with gene knockdown. Briefly, plasmids encoding CVS N, P, and L and the RABV minigenome were reverse-cotransfected into 293T cells in 96-well plates. After 8 h, the cells were transfected with 20 nM of siRNA using Lipofectamine RNAiMAX. Following 70 h of incubation, minigenome replication was evaluated by measuring the luminescence of NanoLuc from the minigenome using Nano-Glo (Promega).

Immunofluorescence assays

RABV-infected cells were fixed with 10% phosphate-buffered formalin and washed with PBS. Blocking was conducted with 1% BSA in PBS for 1 h at room temperature. The cells were then stained with anti-RABV M antibody (A54616; Epigentek; 1:150 dilution) in 0.3% BlockAce in 0.005% Tween-20 in PBS (PBST) overnight at 4°C. After two washes with PBST, Alexa Fluor 594–conjugated anti-rabbit IgG antibody (A32740; Invitrogen; 1:1,000 dilution) was added to the cells as the secondary antibody. The stained cells were observed using an LSM780 confocal microscope and ZEN software (Zeiss).

Electron microscopy analysis

For ultrathin-section electron microscopy, SK-N-SH cells in a collagen-coated dish (10 cm) were infected with rRABV at a MOI of 5–10 and cultured for 28 h. The cells were then washed with phosphate buffer (PB), scraped off the plate, and pelleted *via* centrifugation. The cell pellets were washed, fixed for 30 min with 2.5% glutaraldehyde in PB on ice, and fixed again with freshly prepared fixative at 4°C overnight. The fixed cell pellets were washed with PB and postfixed with 1% osmium tetroxide in PB for 1 h on ice. Subsequent procedures were conducted as described previously[82].

For negative-stain electron microscopy, rRABV purified *via* ultracentrifugation with a 20% sucrose cushion was fixed with 2.5% glutaraldehyde. The fixed virus was placed on an elastic carbon film ELS-C10 (10-1012, Oken) and stained with 2% phosphotungstic acid solution (pH 5.8). The samples were then examined using a H-7650 electron microscope (Hitachi).

Immunoprecipitation assay

First, 293T cells were cotransfected with plasmids encoding FLAG- or HA-tagged TSG101 and RABV M using polyethylenimine. Cell lysates were harvested at 72 h post-transfection, clarified *via* centrifugation. Immunoprecipitation was then conducted using anti-HA magnetic beads (Pierce) according to manufacturer's protocol. The precipitates were extracted into 1x SDS sample buffer containing 2-mercaptethanol and subjected to a standard immunoblotting assay using HRP-conjugated anti-HA antibody (H6533; Sigma; 1:3,000 dilution) and anti-FLAG antibody (A8592; Sigma; 1:3,000 dilution).

Animal experiments

Animal experiments were approved by the Institutional Animal Care and Use Committee of Hokkaido University (approval number 19-0014) and performed according to the committee's guidelines.

Five-week-old male ddY mice were used in the animal experiments. Mice were inoculated intracranially or intramuscularly with 10^2 or 10^5 ffu of rRABV under anesthesia using isoflurane. All mice in the survival groups were observed daily for disease symptoms and BW changes. The humane endpoint was defined as a 20% decrease in BW or an inability to reach food or water due to the onset of disease. Mice were euthanized by decapitation under anesthesia, and their tissues were harvested at specific time points for further analysis.

Immunohistochemistry

Brain sections were prepared as described in the Chapter I. After antigen retrieval in citrate buffer for 5 min using a pressure cooker, the sections were treated with 0.3% H_2O_2 in methanol for 15 min to inactivate endogenous peroxidase. The sections were then treated with 10% goat serum (Nichirei Biosciences) for 1 h at room temperature and incubated at 4℃ overnight with the primary antibody against RABV N (PA321352LA01RAI; Cusabio; 1:2,500 dilution). After three washes with 0.01% PBST, secondary staining was performed with EnVision system-HRP Labelled Polymer Anti-Rabbit (K4220, Dako) for 1 h at room temperature. The slides were washed three times with PBST, and a DAB Substrate Kit (425011, Nichirei) was used to visualize the immunostaining.

Statistical analysis

All statistical analyses were performed using GraphPad Prism 9.2.0. For comparisons of two groups, Welch's *t*-test was used. For comparisons of two groups at

multiple time points, a multiple *t*-test was performed using the Benjamini, Krieger, and Yekutieli method. For comparisons among more than two groups, one-way/two-way ANOVA with Tukey's/Dunnett's multiple comparisons test was used. Data are presented as means ± SD in graphs. **P* < 0.05, ***P* < 0.01, ****P* < 0.001, *****P* < 0.0001.

Results

RNAi screening identifies TSG101 as an ESCRT factor that supports RABV infection

To identify the ESCRT factors involved in RABV growth, ESCRT-knockdown (KD) SK-N-SH cells with a custom siRNA library targeting ESCRT factors were infected with luciferase-expressing RABV, and the progeny virus from the cells was quantified using luciferase assays (Fig. 7A and 7B). Among 25 ESCRTs and their related factors, the KD of *TSG101* was most efficient in terms of decreasing the luciferase signal from progeny RABV in the culture supernatants (Fig. 7B). It was confirmed that the knockdown of *TSG101* significantly decreased the progeny virus titer compared with that detected following the control-siRNA treatment (Fig. 7C). In addition, the RABV titer was reduced in a concentration-dependent manner by the TSG101 inhibitor ilaprazole[83] (Fig. 7D). These results reveal for the first time that TSG101 is a host factor involved in efficient RABV proliferation.

To confirm the TSG101-dependency of RABV infection, a gain-of-function assay was performed by reintroducing TSG101-expressing plasmids into TSG101-KD (TSG-KD) cells. In addition to wild-type (WT) TSG101, three TSG101 mutants were prepared: mutants carrying amino acid substitutions at a ubiquitin-binding site (TSG/N45A) or a PT(/S)AP-binding-site (TSG/M95A), and a mutant lacking a PTAP-motif (TSGΔPTAP), which is involved in recognition by the viral L-domain (Fig. 7E). The exogenous expression of WT TSG101 significantly rescued the virus titer in TSG-KD cells. Among the three TSG101 mutants, the expression of the TSG/M95A mutant resulted in the highest rescue efficacy, whereas the expression of the TSG/N45A and TSGΔPTAP mutants only exerted partial effects on viral growth in TSG-KD cells (Fig. 7F). These results indicate that the ubiquitin-binding site and PTAP-motif in TSG101 would appear to be required for TSG101-mediated RABV growth.

Involvement of TSG101 in the assembly and budding processes of RABV virions

Next, an attempt was made to determine which steps in the RABV life cycle are promoted by TSG101 expression. TSG-KD had no effect on the cellular attachment and entry steps of RABV infection (Fig. 8A and 8B). A minigenome assay showed that replication and gene expression from a RABV minigenome were not affected by the suppression of TSG101 expression (Fig. 8C). Moreover, intracellular viral RNA levels were similar in control and TSG-KD cells until 24 hpi (Fig. 8D). Infectious virions were detected from 12 hpi in both

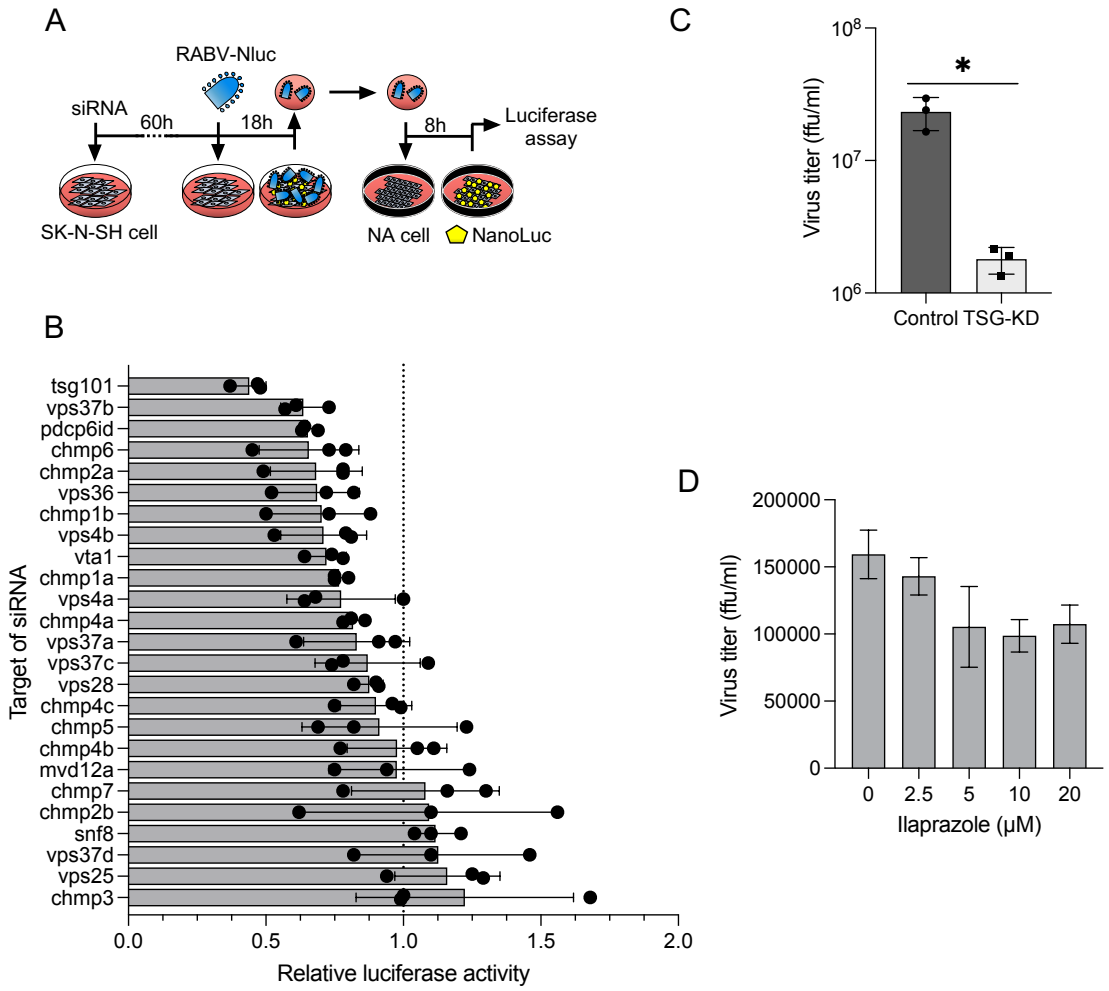

Figure 7. RNAi screening identifies TSG101 as an ESCRT factor supporting RABV infection

(A) Schematic image of the RNAi screening method. siRNA-transfected SK-N-SH cells were infected with RABV-Nluc at a MOI of 10, and culture supernatants collected at 18 hpi were passaged into NA cells. Luciferase activity in the NA cells was measured at 8 hpi. (B) Luciferase activity derived from NanoLuc-encoded reporter RABV in siRNA-treated SK-N-SH cells relative to the luciferase activity in control siRNA-treated cells. Dots indicate the mean of three different siRNAs for each target. Bars indicate the means ± SD of the three siRNAs. (C) Virus titers in the supernatants of TSG-KD SK-N-SH cells at 48 hpi. The titers were measured using a focus forming assay. Bars indicate the means ± SD of three replicates from a representative experiment. (D) Virus titers in the presence of the TSG101 inhibitor ilaprazole. SK-N-SH cells were infected with RABV at a MOI of 1 and cultured with the indicated concentrations of ilaprazole for 24 h. Bars indicate the means ± SD of three replicates from a representative experiment. (Continued on the next page)

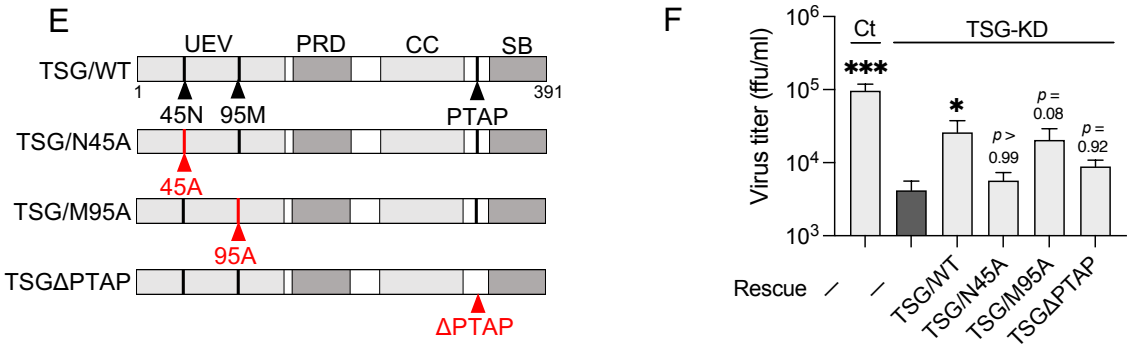

Figure 7. (Continued)

(E) Schematic images of the TSG101 mutants used in this study. Mutation sites are marked in red. UEV: ubiquitin-conjugating enzyme E2 variant; PRD: proline-rich domain; CC: coiled-coil domain; PTAP: conserved PTAP tetrapeptide motif; SB: steadiness box. (F) Virus titers in TSG-KD and rescue cells. TSG-KD cells were transfected with siRNA-resistant TSG101-encoding plasmids and infected with RABV at a MOI of 1. The virus titers in supernatants at 24 hpi were measured. Bars indicate the means ± SD of three replicates from a representative experiment. Ct: control siRNA. Statistical analyses: (C) Welch's *t*-test: **P* < 0.05; (F) one-way ANOVA and Dunn's multiple comparisons tests: **P* < 0.05, ****P* < 0.001.

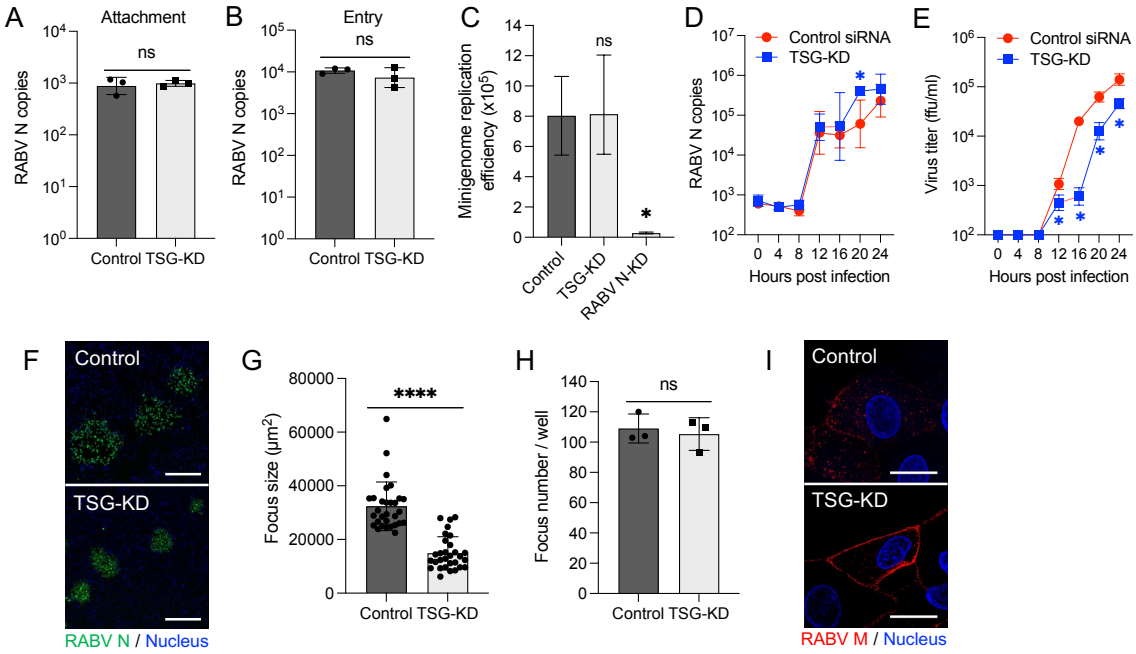

Figure 8. Downregulation of TSG101 expression obstructs the RABV budding process

(A) Virus attachment on the surface of TSG-KD cells. SK-N-SH cells were incubated with RABV at 4°C for 1 h. After the cells were washed, RNA was extracted with attached virions and analyzed using qRT-PCR. (B) Viral entry into TSG-KD cells. SK-N-SH cells were infected with RABV at a MOI of 10. After incubation at 37°C for 30 min, uninternalized virions were removed *via* trypsin treatment. Internalized virions were measured using qRT-PCR. (C) RABV minigenome replication in TSG-KD cells. 293T cells exogenically expressing the RABV minigenome were transfected with siRNA against TSG101. Minigenome replication was evaluated by measuring the luminescence signal from NanoLuc. (D) Viral RNA levels at the early stage of virus infection. Viral RNA levels in TSG-KD SK-N-SH cells were measured at the indicated time points using qRT-PCR. (E) Virus titers at the early stage of virus infection. Virus titers in the supernatants from TSG-KD SK-N-SH cells were measured at the indicated time points. (F, G) Focus size of RABV-infected TSG-KD A549 cells. (F) Foci formed by RABV-infected cells were immunostained with anti-RABV N antibody at 72 hpi. Scale bar: 200 μm. (G) The areas of 30 foci selected randomly were measured using ImageJ. (H) The number of foci in TSG-KD A549 cells. (I) Localization of RABV M in TSG-KD SK-N-SH cells. Cells infected with RABV were immunostained with anti-RABV M antibody at 24 hpi and analyzed using confocal microscopy. Scale bar: 20 μm.
(Continued on the next page)

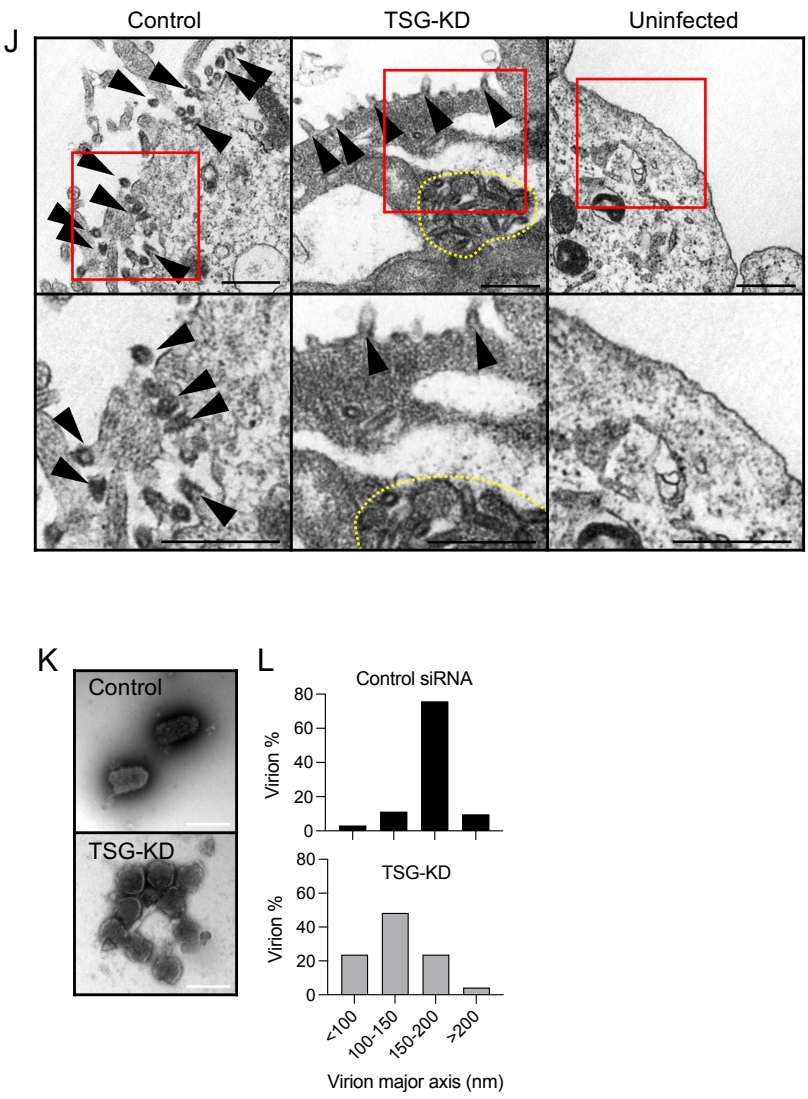

Figure 8. (Continued)

(J) Electron microscopic images of RABV-infected TSG-KD SK-N-SH cells at 28 hpi. Arrow heads: virions; dot line: accumulation of virions. Scale bar: 500 nm. (K) Purified RABV virions were negatively stained and analyzed using electron microscopy. Scale bar: 200 nm. (L) Virion diameter and abundance ratio. Purified RABV virions in 50 images captured randomly with an electron microscope were measured using ImageJ. (A–G) Means ± SD of three replicates from a representative experiment. Statistical analyses: (A, B, G, H) Welch's *t*-test: $*P < 0.05$, $****P < 0.0001$; (C) one-way ANOVA and Dunnett's multiple comparison test: $*P < 0.05$; (D, E) multiple *t*-tests: $*P < 0.05$.

cell lines. The virus titer increased markedly at 16 hpi in control cells, whereas a similar increase occurred 4 h later (i.e., 20 hpi) in TSG-KD cells (Fig. 8E). Additionally, the focus size of RABV-infected TSG-KD cells was significantly decreased compared to that of control cells (Fig. 8F and 8G), in contrast to the number of RABV-infected foci, which was identical under both conditions (Fig. 8H). The accumulation of RABV M and virions was observed beneath the cell membrane using confocal and electron microscope imaging (Fig. 8I and 8J). Notably, viral particles released from TSG-KD cells had a rounded form, which is distinct from the typical bullet shape of RABV virions (Fig. 8K). The length of the major axis was 150–200 nm in WT RABV virions, but the length shifted to 100–150 nm in progeny virions released from TSG-KD cells (Fig. 8L). These results indicate that TSG101 plays a role in the late stage of RABV infection, specifically in virion formation and release as well as subsequent spread to neighboring cells.

TSG101 interacts with the L-domain in RABV M

TSG101 has been reported to interact with the L-domain in the viral proteins of some envelope viruses[74,76,84,85]. RABV possesses two representative L-domains: PxxY(PY) motif (PPEY) and YxxL (YL) motif (YVPL) at amino acid positions 35–38 and 38–41 in the RABV M, respectively (Fig. 9A). Therefore, the interaction between RABV M and TSG101 was examined. In SK-N-SH cells expressing the TSG101–venus fusion protein, RABV M colocalized with TSG101–venus (Fig. 9B). Additionally, when RABV M and TSG101 were co-expressed in 293T cells, they were also shown to interact in co-immunoprecipitation studies (Fig. 9C). To identify the region responsible for the interaction between RABV M and TSG101, RABV M and TSG101 mutants were included in the co-immunoprecipitation assays. RABV M mutants with a substitution in each L-domain (Fig. 9A) showed lower binding affinity to TSG101 (Fig. 9C). In particular, the lack of the YL motif in RABV M led to a marked decrease in the interaction between RABV M and TSG101 (Fig. 9C). Additionally, TSG/N45A (the ubiquitin-binding deficient mutant) showed a lower interaction with RABV M (Fig. 9C). These results suggest that RABV M interacts with TSG101, and their respective L-domain and ubiquitin binding site are the likely target sites for the interactions.

Furthermore, the PY and YL motifs in RABV M are conserved throughout the lineages of RABV (Fig. 10A). As well as the fixed virulent challenge virus standard (CVS) strain, the fixed attenuated HEP strain and street Toyohashi strain exhibited significantly

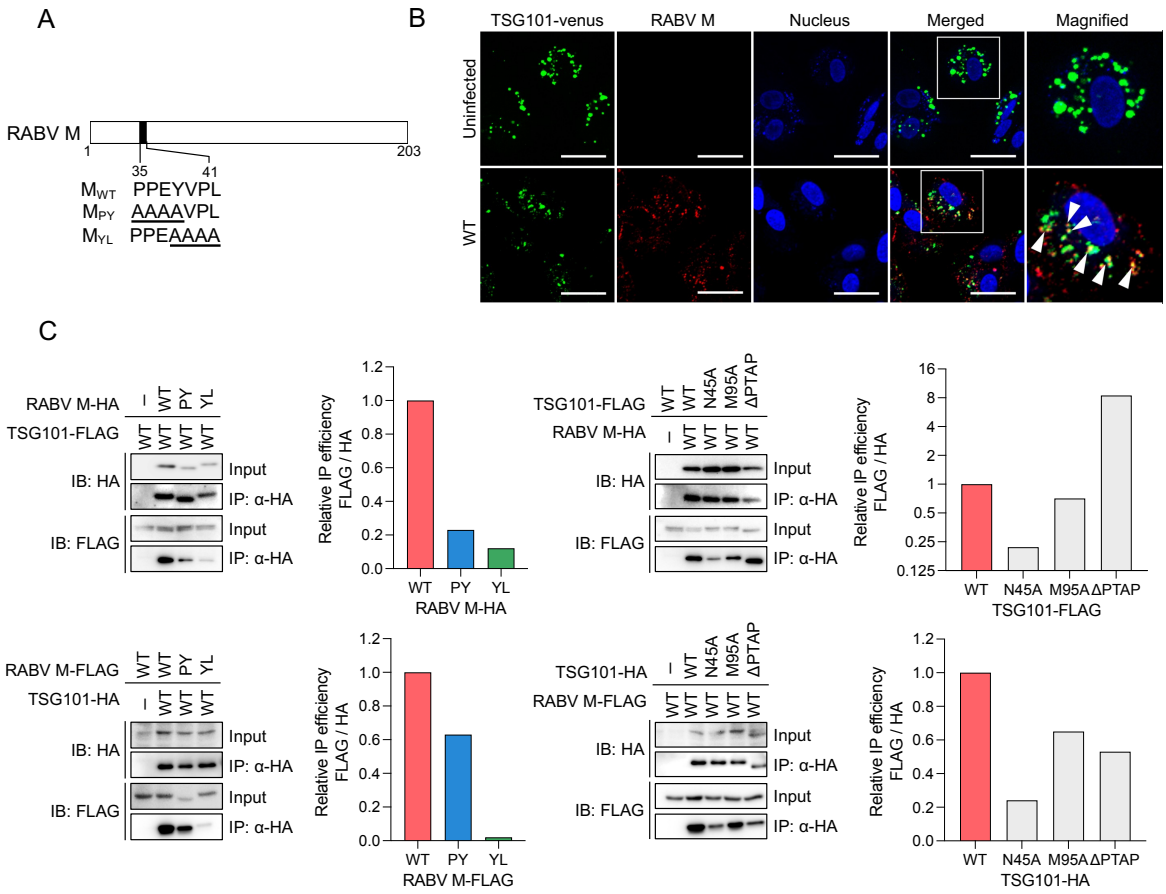

Figure 9. RABV M interacts with TSG101 *via* the L-domain

(A) Schematic representation of RABV M and the L-domain mutants. (B) Colocalization of RABV M and TSG101. SK-N-SH cells stably expressing TSG101–venus were infected with RABV, immunostained with anti-RABV M at 24 hpi, and analyzed using confocal microscopy. Arrow heads show colocalization. Scale bar: 50 μm. (C) Coimmunoprecipitation of RABV M with TSG101. HA- or FLAG-tagged RABV M and TSG101 were coexpressed in 293T cells and coimmunoprecipitated using anti-HA magnetic beads. Immunoblotting was performed with anti-HA or -FLAG antibody. Bar graphs show the relative precipitation efficacy (IP / Input) of FLAG compared with that of HA from a representative experiment following quantification *via* ImageJ.

A

	Lineage	Strain name	27-49th amino acid sequence in RABV M	Accession No.
Fix	Cosmopolitan	CVS	YDDD LWLP **PPEYVPL** KELT SKKN	LC325820
	Cosmopolitan	HEP	DGDD LWLP **PPEYVPL** KELT SKKN	AB085828
	Cosmopolitan	ERA	DDDD LWLP **PPEYVPL** KELT SKKN	AB781935
Street	Cosmopolitan	1088	DDDD LWLP **PPEYVPL** KELT SRKN	AB645847
	Arctic-related	Komatsugawa	DDDD LWLP **PPEYVPL** KELT GKKN	LC553558
	Asia	8743THA	DDDD LWLP **PPEYVPL** KELT GKKN	EU293121
	Asia	Toyohashi	DDDD LWLP **PPEYVPL** KELT SKKN	LC619707.1
	Indian Subcontinent	RY2417	DDDD LWLP **PPEYIPL** KELA GKKN	KF154999
	Africa2	DRV-NG11	DDDD LWLP **PPEYVPL** KELT GKKN	KC196743.1
	RAC-SK	PRV ON-99-2	DDDD LWLP **PPEYVPL** KELT GKKN	EU311738
	Bat	SHBRV-18	DDDD LWLP **PPEYIPL** KEIT GKKN	AY705373

B

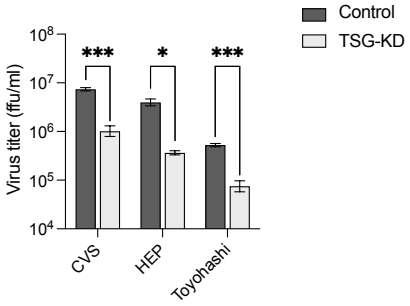

Fig. 10. Conservation and functional importance of the L-domain in various fixed and street strains of RABV

(A) Table listing the 27th to 49th amino acid sequences in RABV M. Bold: L-domain; red: strains analyzed in (B). (B) Virus titers of the CVS strain, HEP fixed strain, and Toyohashi street strain in TSG-KD cells. SK-N-SH cells were infected with RABV at a MOI of 1. Virus titers in the culture supernatants at 48 hpi were determined using a focus forming assay. Bars indicate the means ± SD of three replicates from a representative experiment. Statistical analyses: multiple t-tests with Welch's correction: *P < 0.05, ***P < 0.001.

decreased virus titers in TSG-KD cells (Fig. 10B), suggesting a general function of RABV M–TSG101 interaction in RABV infection.

Mutation at the L-domain disrupts the TSG101-dependent infection of RABV

To further determine the importance of the RABV L-domain in the virus life cycle, replication-competent RABV mutant clones were generated, namely RABV/PY and RABV/YL, in which the PY and YL motifs in RABV M were substituted with alanine, respectively (Fig. 11A). When the growth of the mutants was assessed, the virus titer of RABV/YL was significantly lower than that of RABV/WT and RABV/PY in nontreated control cells; on the other hand, there was no difference among the virus titers in TSG-KD cells (Fig. 11B). The accumulation of RABV M in the peripheral cytoplasm, which was observed in TSG-KD cells infected with RABV/WT (Fig. 11C), was reproduced in control cells infected with RABV/PY and RABV/YL (Fig. 11C). In addition, RABV/PY M and RABV/YL M did not colocalize with TSG101–venus in the infected cells (Fig. 11C). These results suggest that both the PY and YL motifs in the RABV L-domain could mediate the RABV M–TSG101 interaction during viral infection, and the YL motif is more important in the TSG101-dependent RABV life cycle.

Mutation at the L-domain perturbates RABV budding and spread in vitro

RABV/PY and RABV/YL were further characterized to better understand the role of the L-domain in RABV infection. In SK-N-SH cells, the viral growth of RABV/PY was comparable with that of RABV/WT, whereas the growth efficiency of RABV/YL was lower than that of RABV/PY and RABV/WT (Fig. 12A). RABV/WT and the two mutants showed similar trends in viral RNA replication until 24 hpi (Fig. 12B). Although the infectious progeny viruses of RABV/WT and the mutants were detected in the culture supernatants from 12 hpi, RABV/YL showed a considerably lower virus titer after 16 hpi (Fig. 12C). In terms of focus formation, the focus sizes of RABV/PY and RABV/YL were significantly smaller than that of RABV/WT (Fig. 12D and 12E), indicating a low efficiency of virus spread by both mutants. These results indicate that substitutions at the L-domain of RABV M critically decrease viral proliferation. Accompanied by the accumulation of the RABV M along the plasma membrane (Fig. 11C), virus particles remained tethered to the cell surface in RABV/PY and RABV/YL infection, as observed under an electron microscopy (Fig. 12F). Additionally, the accumulation of virions in the cytoplasm of RABV/YL-infected cells was

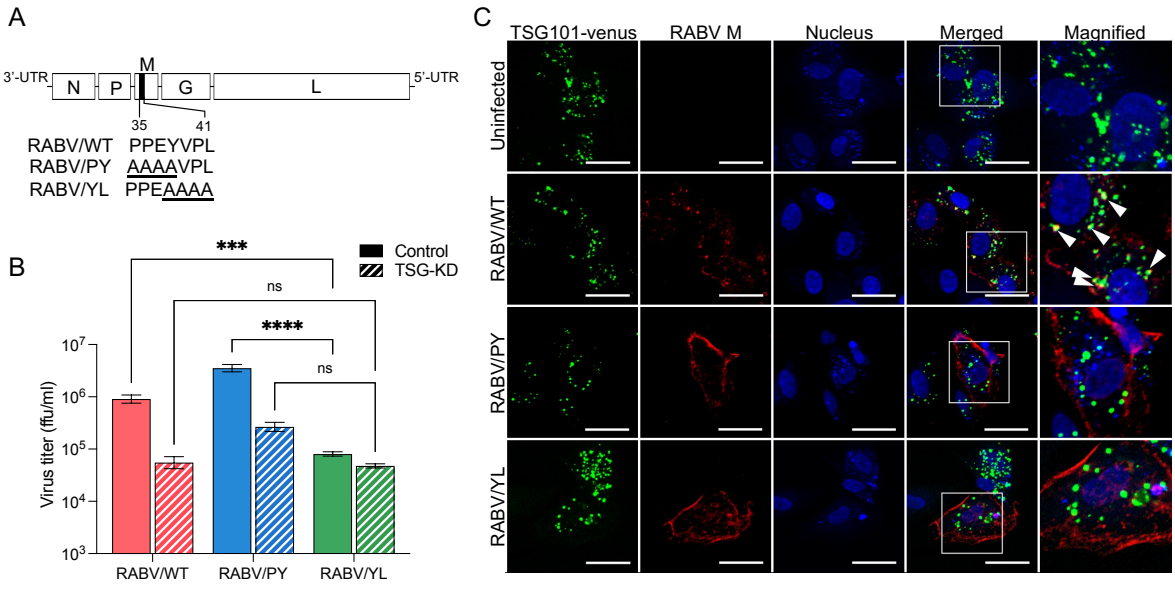

Figure 11. RABV YL motif is essential for TSG101-mediated viral growth

(A) Schematic representation of recombinant RABV with alanine substitutions in the L-domain in RABV M. (B) Virus titers of RABV L-domain mutants. TSG-KD SK-N-SH cells were infected with RABV mutants at a MOI of 1, and virus titers in the supernatants at 48 hpi were measured. Statistical analyses: two-way ANOVA and Sidak's multiple comparisons tests: ***$P < 0.001$, ****$P < 0.0001$. (C) Colocalization of RABV M and TSG101. SK-N-SH cells stably expressing TSG101–venus were infected with RABV, immunostained with anti-RABV M at 24 hpi, and analyzed using confocal microscopy. Arrow heads show colocalization. Scale bar: 50 μm.

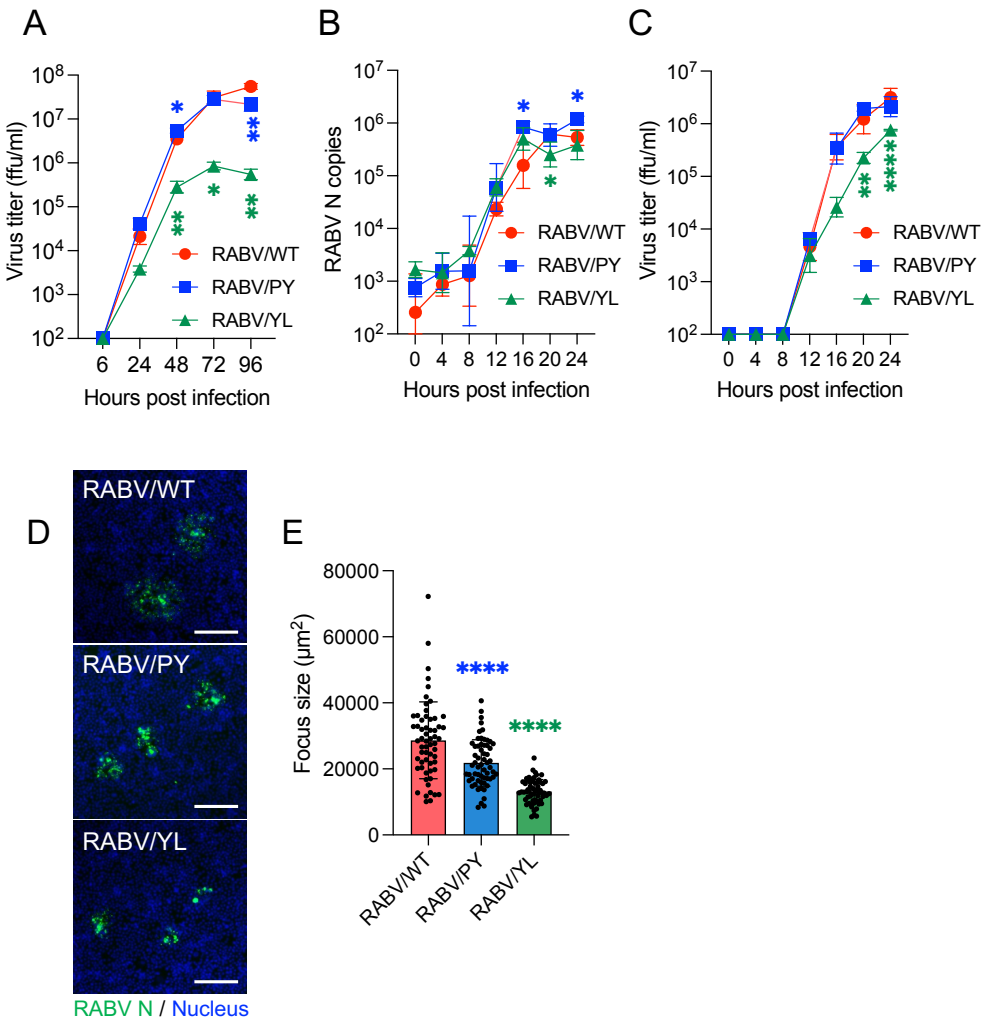

Figure 12. Impaired growth of RABV L-domain mutants

(A) Virus growth curves in SK-N-SH cells during a multicycle infection. Cells were infected with RABV at a MOI of 0.01, and virus titers in the supernatants were measured at the indicated time points. (B) Viral RNA levels at the early stage of virus infection in SK-N-SH cells. Cells were infected with RABV at a MOI of 1, and virus replication in the cells was evaluated at the indicated time points using qRT-PCR. (C) Virus titers at the early stage of virus infection in SK-N-SH cells. Cells were infected with RABV at a MOI of 1, and virus titers in the supernatants were measured at the indicated time points. (D, E) Focus size of RABV L-domain mutants. The areas of 60 foci selected randomly in NA cells were measured using ImageJ. (Continued on the next page)

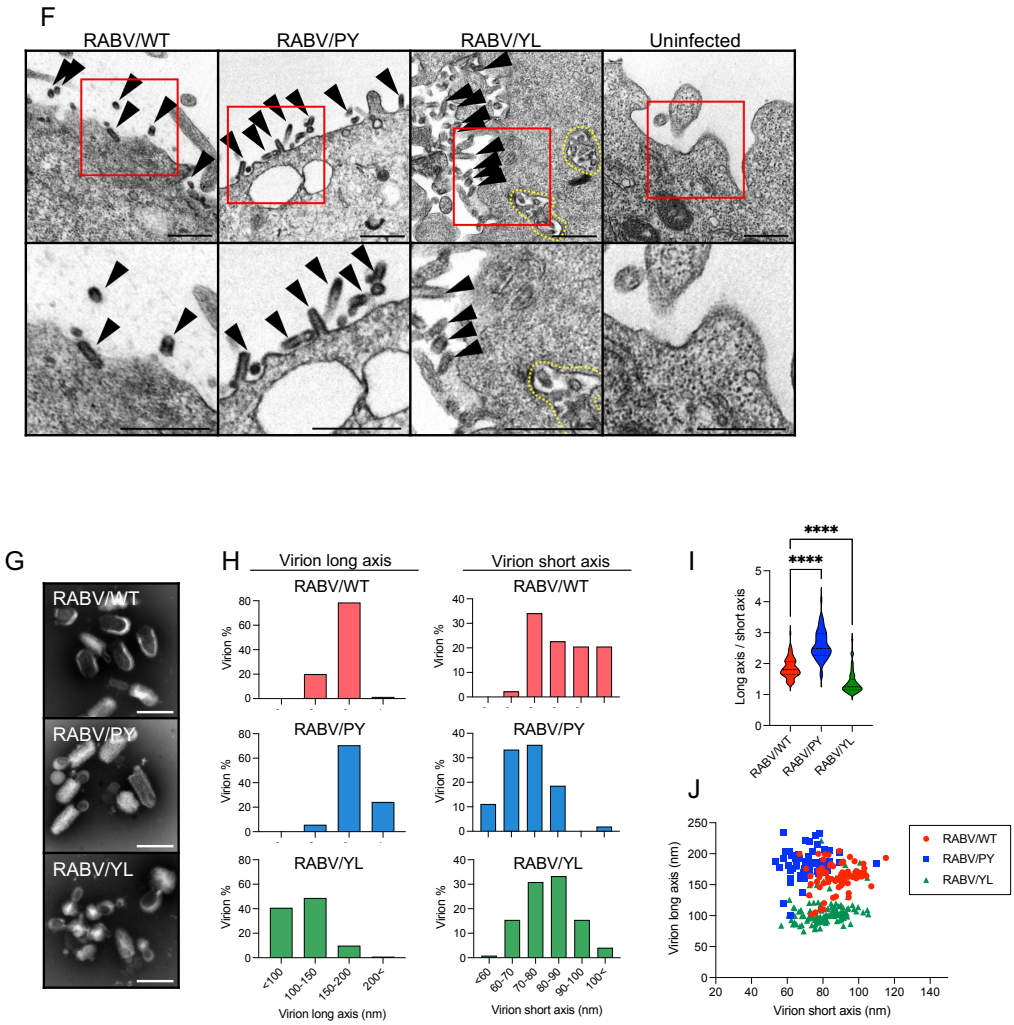

Figure 12. (Continued)

(F) Electron microscopy images of SK-N-SH cells at 28 hpi of RABV L-domain mutants. Arrow heads: virions; dot line: accumulation of virions. Scale bar: 500 nm. (G) Purified virions of RABV L-domain mutants were negatively stained and analyzed using electron microscopy. Scale bar: 200 nm. (H–J) Purified RABV virions in 50 images captured randomly with an electron microscope were measured using ImageJ. (H) Abundance ratio of virion diameter in long axis and short axis. (I) Ratio of long axis to short axis of virions. The middle dot lines indicate median, top and bottom dot lines indicate quartile. (J) Length of long axis and short axis of each individual virions. (A–C) Means ± SD of three replicates from a representative experiment. Statistical analyses: (A–C) multiple *t*-tests: $*P < 0.05$, $**P < 0.01$, $****P < 0.0001$. (E, I) One-way ANOVA and Dunnett's multiple comparison test: $****P < 0.0001$.

observed (Fig. 12F). In terms of virion morphology, RABV/PY had slightly thinner and longer virions compared with those of RABV/WT, whereas RABV/YL formed rounded particles that clearly differed from the representative bullet-like particles of rhabdoviruses (Fig. 12G–J). Notably, the characteristics of RABV/YL were consistent with those of RABV/WT in TSG-KD cells (Fig. 8D–L). These results suggest that the L-domain, especially the YL motif, in the RABV M plays an essential role in RABV budding and bullet-like virus particle formation.

Pathogenicity of RABV L-domain mutants in vivo

To determine the influence of the L-domain on RABV pathogenicity *in vivo*, mice were intracranially or intramuscularly infected with the RABV L-domain mutants. Intracerebral inoculation showed a 1- and 2-day delay in the survival curve and body weight loss for RABV/PY and RABV/YL mutants, respectively (Fig. 13A and 13B). The virus titers of both mutants in the brain at 4 dpi were similar, and they were ~80-fold lower than that observed with the parental RABV/WT (Fig. 13C). Viral proteins were distributed extensively across the whole brain of RABV/WT-infected mice, whereas infection was limited in the brains of mice infected with RABV/PY and RABV/YL (Fig. 13D). Even on 6 dpi, virus growth and distributions of RABV/PY and RABV/YL were limited compared to those of RABV/WT at 4 dpi, whereas the mice were on the similar disease progressions (Fig. 13E and 13F). Following intramuscular inoculation, both mutants had a 2-day delay in the survival curve and body weight change compared with the control (Fig. 13G and 13H). In terms of virus propagation, the virus titer in the brain was 34.8-fold lower for RABV/PY and 509.6-fold lower for RABV/YL compared with the control virus titer (Fig. 13I). Although the disease progression of mice infected with either mutant was similar, there was a marked difference between the virus titers of the two mutants (Fig. 13I). These results suggest that the substitution of the L-domain results in the attenuation of RABV, indicating the importance of both the PY and YL motifs in RABV replication not only *in vitro* but also *in vivo*.

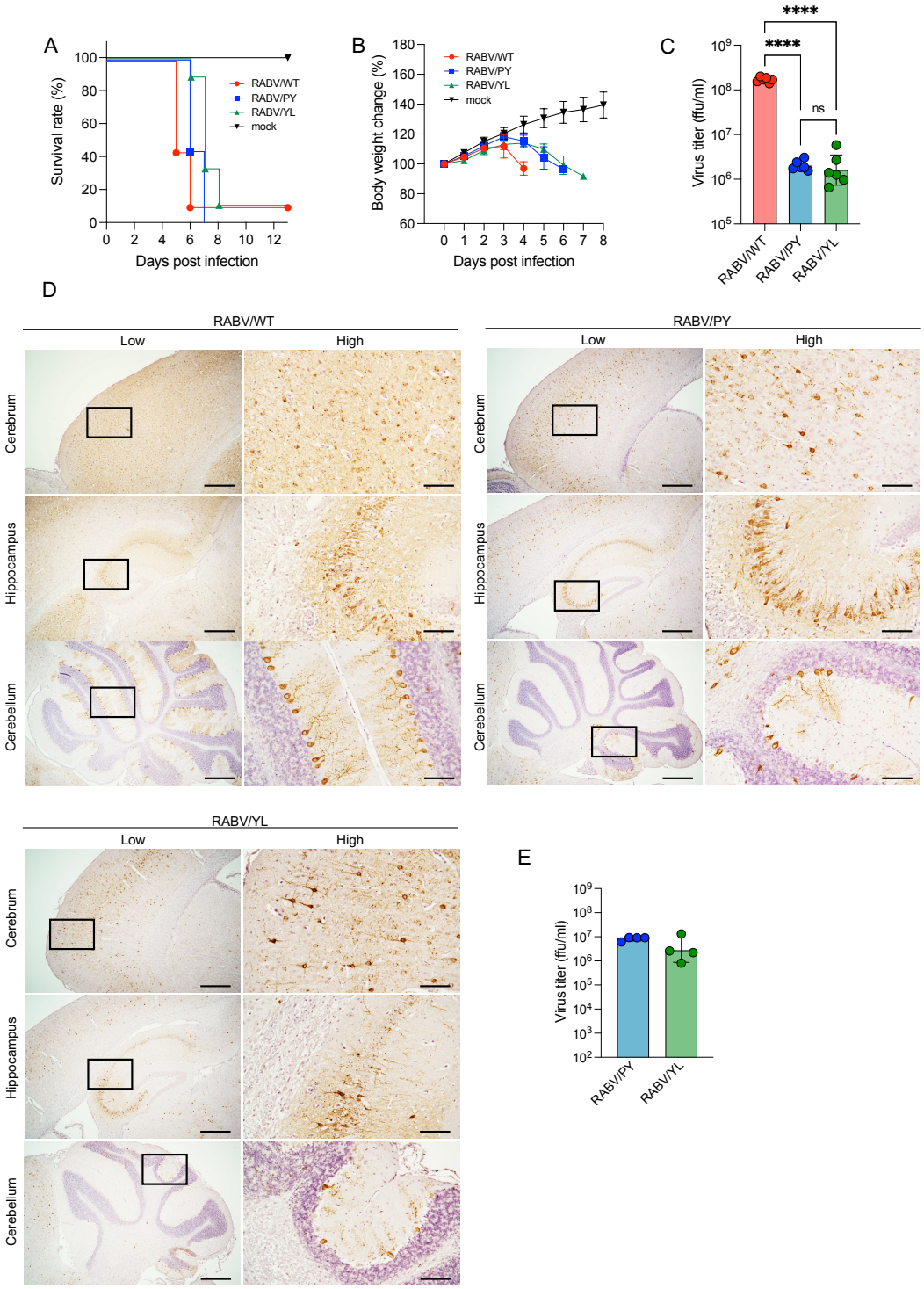

Figure 13. (Continued on the next page)

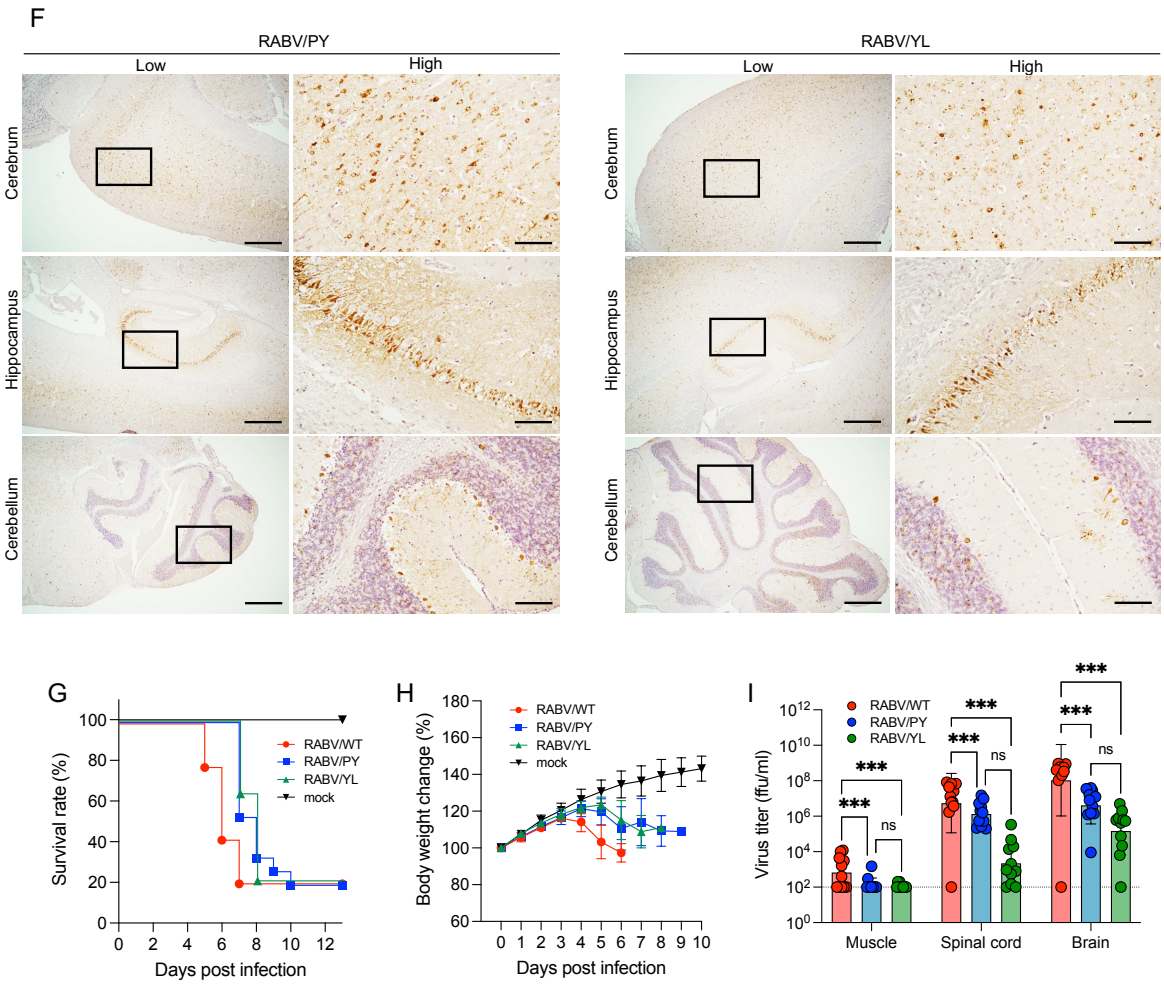

Figure 13. Attenuation of RABV L-domain mutants *in vivo* (Continued)

Five-week-old ddY mice were inoculated with 10^2 or 10^5 ffu RABV intracranially (A–F) or intramuscularly (G–I). Virus-infected mice were monitored for (A, G) survival and (B, H) body weight changes. Data in the graphs are means ± SD [mock: n = 6 (ic), n = 6 (im); RABV/WT: n = 8 (ic), n = 14 (im); RABV/PY: n = 9 (ic), n = 15 (im); RABV/YL: n = 9 (ic), n = 14 (im)]. (C, E, I) Virus titers in tissue homogenates at 4 dpi (ic), 6 dpi (ic) or 5 dpi (im) were determined using a focus forming assay. Bars show means ± SD [n = 6 (4 dpi, ic), n = 4 (6 dpi, ic) and n =11 (im) for each group]. (D, F) Immunohistochemistry of the mouse brain. Brain sections at 4 dpi (D) and 6 dpi (F) were stained with anti-RABV N. Scale bars: 500 μm (low magnification) and 100 μm (high magnification). Statistical analyses: (C, I) one-way ANOVA and Tukey's multiple *t*-tests: ***$P < 0.001$, ****$P < 0.0001$.

Discussion

Virus budding is a sophisticated process required for infectious viral particle production and release. In rhabdovirus infection, the M protein is essential for budding and the formation of typical bullet-shaped particles, given that M-deficient viruses form long filamentous particles that are not infective[20]. RABV M also has multiple functions at the late stage of RABV infection, when it is involved in the condensation and assembly of RNPs as well as the pushing out and pinching off of viral particles[20,66–69,86]. However, little is known about the host factors involved in the budding and particle formation processes of rhabdoviruses. In chapter II, the RNAi screen identified TSG101 as an ESCRT factor that supports RABV infection. Moreover, these experiments demonstrated that TSG101 facilitates RABV budding and virion formation.

The ESCRTs play roles in membrane scission, which is a crucial process in cytokinesis[71,73] and the formation of endosomal luminal vesicles and exosomes[72]. ESCRT-mediated membrane invagination and vesicle formation is a process analogous to the budding step during the release of virions from cells. Some enveloped viruses, such as retroviruses, filoviruses, paramyxoviruses, and flaviviruses, are reported to use the ESCRT in viral particle budding[74,76,84,85]. In the present study, RABV growth was significantly impaired by TSG-KD (Fig. 7C); however, the knockdown of TSG101 had no effect on viral entry, genome replication, and protein synthesis (Fig. 8A–D), although it caused the intracellular accumulation of viral particles and the distortion of virion morphology (Fig. 8I–L). These results provide evidence that TSG101 contributes to the late stage of RABV infection, specifically virion assembly and budding.

L-domains are consensus amino acid sequences observed in the structural proteins of various viruses and are known to be involved in the recruitment of ESCRTs[87]. RABV possesses an L-domain composed of overlapping PY and YL motifs (PPEYVPL) at amino acid positions 38–41 in RABV M. Amino acid substitutions of the PY motif in RABV M are reported to decrease the growth and pathogenicity of RABV; however, the molecular mechanisms underlying this attenuation remain to be elucidated[78]. In the current study, it has been demonstrated that TSG101 interacts with RABV M *via* the L-domain, which is required for the colocalization of these proteins (Figs. 9B and 11C). Recombinant RABVs lacking the L-domain in RABV M show low viral proliferation and pathogenicity both *in vitro* and *in vivo* (Fig. 12A, 13A–D, and 13G–I). Notably, the RABV/YL mutant showed an impaired budding ability leading to an abnormal particle morphology (Fig. 12G–J). Meanwhile, the

lack of PY motifs resulted in formation of longer and thinner viral particles, inhibition of cell-to-cell infection, and reduction in pathogenicity in mice (Fig. 12D–J, 13A–D, and 13G–I), suggesting that this motif may contribute to RABV infection differently from the YL motif. Collectively, these results revealed an important function of the L-domain, especially the YL motif, in the TSG-dependent RABV life cycle. In contrast vesicular stomatitis virus, a prototype rhabdovirus, has been shown only to possess the PY motif in its M, and it is reportedly less dependent on TSG101 for viral growth[88].

The binding mode of TSG101 to RABV M remains to be elucidated. In addition to constructing complexes with other ESCRTs, the key functions of TSG101 in endocytic trafficking are mediated by binding to one of the L-domains, i.e., to P(T/S)AP motif-containing proteins *via* methionine at position 95 (95M) or to ubiquitin *via* asparagine at position 45 (45N)[73,89–91]. None of the RABV proteins possess the P(T/S)AP motif, and the rescue experiments (Fig. 7F) and immunoprecipitation assays (Fig. 9C) suggest that 95M in TSG101 is not required for RABV replication. However, the introduction of an amino acid mutation on 45N (TSG/N45A) resulted in a poor RABV growth rescue rate (Fig. 7F) and a weakened RABV M binding capacity (Fig. 9C). Considering the role played by ubiquitin in triggering cell membrane invagination for endocytosis[92], the involvement of ubiquitin in virus budding appears plausible[76,93–96]. During rhabdovirus infection, M is also ubiquitinated by the host E3 ubiquitin ligase[93,95]. Based on the present data and previous studies, it is speculated that the ubiquitination of RABV M might facilitate the RABV M–TSG101 interaction.

In summary, this study has revealed that TSG101 supports the budding and formation of RABV viral particles through its interaction with RABV M *via* the L-domain. Considering the involvement of host factors in RABV infection, the discovery of a host factor that plays a critical role in the egress of RABV provides new insights into the mechanisms of RABV budding and virion formation, especially as it highlights the importance of the L-domain in RABV M. In future studies, focusing on the involvement of other ESCRT factors and ubiquitin will improve the understanding of the mechanisms underlying RABV budding and the production of bullet-shaped virion formation and may help integrate previously disconnected studies.

Conclusion

Rabies is a viral zoonosis of international public health importance that needs to be addressed. There are many questions about the mechanism of RABV infection, propagation, and pathological manifestation, and it is required to accumulate sufficient knowledge to develop effective therapeutics.

In Chapter I, the attenuation mechanism dependent on the 333rd amino acid residue of the G protein of HEP strain, an attenuated vaccine strain of RABV, was investigated. The vaccine strain HEP with Glu at G333 does not exhibit pathogenicity in mice, but the HEP^{333}R strain in which G333 is replaced with Arg becomes lethally pathogenic in mice. Underlying this pathogenetic difference, the HEP strain had a higher astrocyte infection efficiency and a higher level of IFN production in astrocytes than the HEP^{333}R strain. Strong relationship between the accelerated IFN response and pathogenesis associated with astrocyte infection was confirmed by lethal phenotype of HEP strain in type I and type II IFN receptor-deficient mice (AG129 mice). Thus, it is shown that the IFN response in infected astrocytes is important for elimination of HEP strains resulting in attenuation.

Chapter II focused on the virus-host interaction, which is essential for understanding the viral life cycle, and analyzed the role of ESCRT factors generally involved in lipid membrane modeling. In this chapter, the ESCRT-I member TSG101 was revealed to interact with the M protein *via* the L-domain and contributes to RABV budding and particle formation. Suppression of TSG101 expression or impaired RABV mutant binding to TSG101 showed common abnormalities such as intracellular aggregation of viral proteins and disruption of the bullet-like viral particles. Furthermore, this RABV mutant reduced proliferation in cells and virulence in mice. These results suggest that the RABV budding and bullet-shaped virus particle formation are highly dependent on TSG101, and that the RABV M-TSG101 interaction *via* the L-domain is important for this process and efficient virus replication.

Finally, in this study, new mechanisms for virulence manifestation/attenuation and a molecular mechanism for budding and bullet-shaped particle formation of RABV was proposed. Understanding pathogenicity and attenuation mechanisms is important for the development and improvement of live attenuated vaccines, which is a key to control rabies in wild animals [2,3]. Also, clarifying virus-host interactions is essential to understand the host-dependent viral infection cycle. I hope these findings will encourage further research to understand the molecular mechanisms of RABV infection and virulence, and future research will expand the potential therapeutic targets for rabies.

Acknowledgments

My great appreciation is extended to my supervisors Professor Hirofumi Sawa, Associate Professor Yasuko Orba, and Lecturer Michihito Sasaki (Division of Molecular Pathobiology, International Institute for Zoonosis Control, Hokkaido University) for their persevering guidance. I would like to extent my graduate to Professor Hiroaki Kariwa (Laboratory of Public Health, Faculty of Veterinary Medicine, Hokkaido University), Associate Professor Keita Matsuno (Division of Risk Analysis and Management, International Institute for Zoonosis Control, Hokkaido University), and Professor William W. Hall (University College of Dublin) for their intellectual discussion and critical reading of this thesis.

I would like to appreciate Dr. Takeshi Saito, Professor Ayato Takada (Division of Global Epidemiology, International Institute for Zoonosis Control, Hokkaido University), Associate Professor Shintaro Kobayashi (Laboratory of Public Health, Faculty of Veterinary Medicine, Hokkaido University), Professor Naoto Ito (Gifu University), Dr. Michiko Harada, Dr. Satoshi Inoue, Dr. Ken Maeda, Dr. Chang-Kweng Lim (National Institute of Infectious Diseases), Dr. Akihiko Kawai (Research Institute for Production and Development), Mr. Takashi Namba, Associate Professor Osamu Ichii, and Professor Yasuhiro Kon (Laboratory of Anatomy, Faculty of Veterinary Medicine, Hokkaido University) for their kind offer of experimental materials and technical supports.

I would also like to thank my laboratory members for major supports on this study. Especially for my colleagues, Mr. Koshiro Tabata and Ms. Mai Kishimoto, I greatly appreciate that we have supported and learned from each other as good friends.

My graduate school days and Ph.D. studies were financially supported by the Japan Society for the Promotion of Science (JSPS) KAKENHI under grant numbers 18H02333, 18KK0192, 21J13419; the Japan Agency for Medical Research and Development (AMED) under grant number JP22fk0108141; Health Labour Sciences Research under grant number 22HA0601; and the World-leading Innovative and Smart Education (WISE) Program from the Ministry of Education, Culture, Sports, Science, and Technology (MEXT) (1801).

References

1. Hampson, K. *et al.* Estimating the Global Burden of Endemic Canine Rabies. *PLoS Negl Trop Dis* **9**, e0003709 (2015).
2. World Health Organization. WHO Expert Consultation on Rabies: Third report. (2018).
3. World Health Organization. WHO Expert Consultation on Rabies: Second report. (2013).
4. Yamamoto, S., Iwasaki, C., Oono, H., Ninomiya, K. & Matsumura, T. The first imported case of rabies into Japan in 36 years: A forgotten life-threatening disease. *J Travel Med* **15**, 372–374 (2008).
5. Rare case of canine rabies diagnosed near Paris. Radio France Internationale (RFI). https://www.rfi.fr/en/france/20221028-rare-canine-rabies-case-discovered-near-paris (2022).
6. Albert, V. Rabid fox euthanized after allegedly biting 9 people on Capitol Hill. *CBS NEWS*, https://www.cbsnews.com/news/fox-capitol-hill-euthanized-after-allegedly-biting-9-people/ (2022).
7. Nosaki, Y. *et al.* Fourth imported rabies case since the eradication of rabies in Japan in 1957. *J Travel Med* **28**, 1–4 (2021).
8. Singh, R. *et al.* Rabies – Epidemiology, pathogenesis, public health concerns and advances in diagnosis and control: A comprehensive review. *Vet Q* **37**, 212–251 (2017).
9. Fekadu, M., Shaddock, J. H. & Baer, G. M. Excretion of Rabies Virus in the Saliva of Dogs. *J Infect Dis* **145**, 715–719 (1982).
10. Tsiang, H. Evidence for an Intraaxonal Transport of Fixed and Street Rabies Virus. *J Neuropathol Exp Neurol* **38**, 289–296 (1979).
11. Tsiang, H., Ceccaldi, P. E. & Lycke, E. Rabies virus infection and transport in human sensory dorsal root ganglia neurons. *J Gen Virol* **72**, 1191–1194 (1991).
12. Tsiang, H. Neuronal Function Impairment in Rabies-infected Rat Brain. *J Gen Virol* **61**, 277–281 (1982).
13. Scott, C. A., Rossiter, J. P., Andrew, R. D. & Jackson, A. C. Structural Abnormalities in Neurons Are Sufficient To Explain the Clinical Disease and Fatal Outcome of Experimental Rabies in Yellow Fluorescent Protein-Expressing Transgenic Mice. *J Virol* **82**, 513–521 (2008).
14. Kammouni, W. *et al.* Rabies virus phosphoprotein interacts with mitochondrial Complex I and induces mitochondrial dysfunction and oxidative stress. *J Neurovirol* **21**, 370–382 (2015).
15. Mahadevan, A., Suja, M. S., Mani, R. S. & Shankar, S. K. Perspectives in Diagnosis and Treatment of Rabies Viral Encephalitis: Insights from Pathogenesis. *Neurotherapeutics* **13**, 477–492 (2016).
16. Finke, S. & Conzelmann, K. K. Replication strategies of rabies virus. *Virus Res* **111**,

120–131 (2005).
17. Brzózka, K., Finke, S. & Conzelmann, K.-K. Identification of the Rabies Virus Alpha/Beta Interferon Antagonist: Phosphoprotein P Interferes with Phosphorylation of Interferon Regulatory Factor 3. *J Virol* **79**, 7673–7681 (2005).
18. Vidy, A., Chelbi-Alix, M. & Blondel, D. Rabies Virus P Protein Interacts with STAT1 and Inhibits Interferon Signal Transduction Pathways. *J Virol* **79**, 14411–14420 (2005).
19. Ito, N. *et al.* Role of Interferon Antagonist Activity of Rabies Virus Phosphoprotein in Viral Pathogenicity. *J Virol* **84**, 6699–6710 (2010).
20. Mebatsion, T., Weiland, F. & Conzelmann, K.-K. Matrix Protein of Rabies Virus Is Responsible for the Assembly and Budding of Bullet-Shaped Particles and Interacts with the Transmembrane Spike Glycoprotein G. *J Virol* **73**, 242–250 (1999).
21. Finke, S., Mueller-Waldeck, R. & Conzelmann, K. -K. Rabies virus matrix protein regulates the balance of virus transcription and replication. *J Gen Virol* **84**, 1613–1621 (2003).
22. Morimoto, K., Hooper, D. C., Spitsin, S., Koprowski, H. & Dietzschold, B. Pathogenicity of Different Rabies Virus Variants Inversely Correlates with Apoptosis and Rabies Virus Glycoprotein Expression in Infected Primary Neuron Cultures. *J Virol* **73**, 510–518 (1999).
23. Ito, N., Takayama, M., Yamada, K., Sugiyama, M. & Minamoto, N. Rescue of Rabies Virus from Cloned cDNA and Identification of the Pathogenicity-Related Gene: Glycoprotein Gene Is Associated with Virulence for Adult Mice. *J Virol* **75**, 9121–9128 (2001).
24. Morimoto, K., Foley, H. D., Mcgettigan, J. P., Schnell, M. J. & Dietzschold, B. Reinvestigation of the role of the rabies virus glycoprotein in viral pathogenesis using a reverse genetics approach. *J Neurovirol* **6**, 373–381 (2000).
25. Tao, L. *et al.* Molecular Basis of Neurovirulence of Flury Rabies Virus Vaccine Strains: Importance of the Polymerase and the Glycoprotein R333Q Mutation. *J Virol* **84**, 8926–8936 (2010).
26. Takayama-Ito, M. *et al.* A highly attenuated rabies virus HEP-Flury strain reverts to virulent by single amino acid substitution to arginine at position 333 in glycoprotein. *Virus Res* **119**, 208–215 (2006).
27. Thoulouze, M.-I. *et al.* The Neural Cell Adhesion Molecule Is a Receptor for Rabies Virus. *J Virol* **72**, 7181–7190 (1998).
28. Tuffereau, C., Bé Né Jean, J., Blondel, D., Kieffer, B. & Flamand, A. Low-affinity nerve-growth factor receptor (P75NTR) can serve as a receptor for rabies virus. *EMBO J* **17**, 7250–7259 (1998).
29. Wang, J. *et al.* Metabotropic glutamate receptor subtype 2 is a cellular receptor for rabies virus. *PLoS Pathog* **14**, e1007189 (2018).

30. Sasaki, M. *et al.* The role of heparan sulfate proteoglycans as an attachment factor for rabies virus entry and infection. *J Infect Dis* **217**, 1740–1749 (2018).
31. Gaudin, Y. *et al.* Reversible Conformational Changes and Fusion Activity of Rabies Virus Glycoprotein. *J Virol* **65**, 4853–4859 (1991).
32. Morimoto, K. *et al.* Genetic engineering of live rabies vaccines. *Vaccine* **19**, 3543–3551 (2001).
33. Shuai, L. *et al.* Genetically modified rabies virus ERA strain is safe and induces long-lasting protective immune response in dogs after oral vaccination. *Antiviral Res* **121**, 9–15 (2015).
34. Nakagawa, K. *et al.* Generation of a live rabies vaccine strain attenuated by multiple mutations and evaluation of its safety and efficacy. *Vaccine* **30**, 3610–3617 (2012).
35. Ito, N. *et al.* Safety enhancement of a genetically modified live rabies vaccine strain by introducing an attenuating Leu residue at position 333 in the glycoprotein. *Vaccine* **39**, 3777–3784 (2021).
36. Dietzschold, B. *et al.* Differences in Cell-to-Cell Spread of Pathogenic and Apathogenic Rabies Virus In Vivo and In Vitro. *J Virol* **56**, 12–18 (1985).
37. Faber, M. *et al.* Overexpression of the Rabies Virus Glycoprotein Results in Enhancement of Apoptosis and Antiviral Immune Response. *J Virol* **76**, 3374–3381 (2002).
38. Potratz, M. *et al.* Astrocyte Infection during Rabies Encephalitis Depends on the Virus Strain and Infection Route as Demonstrated by Novel Quantitative 3D Analysis of Cell Tropism. *Cells* **9**, 412 (2020).
39. Mori, T. & Morimoto, K. Rabies virus glycoprotein variants display different patterns in rabies monosynaptic tracing. *Front Neuroanat* **7**, 1–12 (2014).
40. Pfefferkorn, C. *et al.* Abortively Infected Astrocytes Appear To Represent the Main Source of Interferon Beta in the Virus-Infected Brain. *J Virol* **90**, 2031–2038 (2016).
41. Tian, B. *et al.* Lab-attenuated rabies virus causes abortive infection and induces cytokine expression in astrocytes by activating mitochondrial antiviral-signaling protein signaling pathway. *Front Immunol* **8**, 1–17 (2018).
42. Hwang, M. & Bergmann, C. C. Alpha/Beta Interferon (IFN-α/β) Signaling in Astrocytes Mediates Protection against Viral Encephalomyelitis and Regulates IFN-γ-Dependent Responses. *J Virol* **92**, e01901-17 (2018).
43. Detje, C. N. *et al.* Upon Intranasal Vesicular Stomatitis Virus Infection, Astrocytes in the Olfactory Bulb Are Important Interferon Beta Producers That Protect from Lethal Encephalitis. *J Virol* **89**, 2731–2738 (2015).
44. Kallfass, C. *et al.* Visualizing Production of Beta Interferon by Astrocytes and Microglia in Brain of La Crosse Virus-Infected Mice. *J Virol* **86**, 11223–11230 (2012).
45. Weinmann, E., Majer, M. & Hilfenhaus, J. Intramuscular and/or Intralumbar

Postexposure Treatment of Rabies Virus-Infected Cynomolgus Monkeys with Human Interferon. *Infect Immun* **24**, 24–31 (1979).

46. Postic, B. & Fenje, P. Effect of Administered Interferon on Rabies in Rabbits. *Appl Microbiol* **22**, 428–431 (1971).
47. Ito, N. *et al.* Improved recovery of rabies virus from cloned cDNA using a vaccinia virus-free reverse genetics system. *Microbiol Immunol* **47**, 613–617 (2003).
48. Anindita, P. D. *et al.* Generation of recombinant rabies viruses encoding NanoLuc luciferase for antiviral activity assays. *Virus Res* **215**, 121–128 (2016).
49. Milligan, G. N. *et al.* A lethal model of disseminated dengue virus type 1 infection in AG129 mice. *J Gen Virol* **98**, 2507–2519 (2017).
50. Aliota, M. T. *et al.* Characterization of Lethal Zika Virus Infection in AG129 Mice. *PLoS Negl Trop Dis* **10**, e0004682 (2016).
51. Tan, G. K. *et al.* A non mouse-adapted dengue virus strain as a new model of severe dengue infection in AG129 mice. *PLoS Negl Trop Dis* **4**, e672 (2010).
52. Honda, Y., Kawai, A. & Matsumotot, S. Comparative Studies of Rabies and Sindbis Virus Replication in Human Neuroblastoma (SYM-I) Cells that Can Produce Interferon. *J Gen Virol* **65**, 1645–1653 (1984).
53. Préhaud, C., Lay, S., Dietzschold, B. & Lafon, M. Glycoprotein of Nonpathogenic Rabies Viruses Is a Key Determinant of Human Cell Apoptosis. *J Virol* **77**, 10537–10547 (2003).
54. Sarmento, L., Li, X. Q., Howerth, E., Jackson, A. C. & Fu, Z. F. Glycoprotein-mediated induction of apoptosis limits the spread of attenuated rabies viruses in the central nervous system of mice. *J Neurovirol* **11**, 571–581 (2005).
55. Seif, I., Coulon, P., Rollin, P. E. & Flamand, A. Rabies Virulence: Effect on Pathogenicity and Sequence Characterization of Rabies Virus Mutations Affecting Antigenic Site III of the Glycoprotein. *J Virol* **53**, 926–934 (1985).
56. Tuffereau, C. *et al.* Arginine or Lysine in Position 333 of ERA and CVS Glycoprotein Is Necessary for Rabies Virulence in Adult Mice. *Virology* **172**, 206–212 (1989).
57. Lentz, T. L., Wilson, P. T., Hawrot, E. & Speicher, D. W. Amino Acid Sequence Similarity between Rabies Virus Glycoprotein and Snake Venom Curaremimetic Neurotoxins. *Science* **226**, 847–848 (1984).
58. Lentz, T. L., Burrage, T. G., Smith, A. L., Crick, J. & Tignor, G. H. Is the Acetylcholine Receptor a Rabies Virus Receptor? *Science* **215**, 182–184 (1982).
59. Langevin, C., Jaaro, H., Bressanelli, S., Fainzilber, M. & Tuffereau, C. Rabies virus glycoprotein (RVG) is a trimeric ligand for the N-terminal cysteine-rich domain of the mammalian p75 neurotrophin receptor. *J Biol Chem* **277**, 37655–37662 (2002).
60. Marié, I., Durbin, J. E. & Levy, D. E. Differential viral induction of distinct interferon-α genes by positive feedback through interferon regulatory factor-7. *EMBO J* **17**,

6660–6669 (1998).
61. Sato, M. *et al.* Positive feedback regulation of type I IFN genes by the IFN-inducible transcription factor IRF-7. *FEBS J* **441**, 106–110 (1998).
62. Yan, X., Mohankumar, P. S., Dietzschold, B., Schnell, M. J. & Fu, Z. F. The rabies virus glycoprotein determines the distribution of different rabies virus strains in the brain. *J Neurovirol* **8**, 345–352 (2002).
63. Coulon, P., Ternaux, J.-P., Flamand, A. & Tuffereau, C. An Avirulent Mutant of Rabies Virus Is Unable To Infect Motoneurons In Vivo and In Vitro. *J Virol* **72**, 273–278 (1998).
64. Klein, A. *et al.* Comparative pathogenesis of different phylogroup I bat lyssaviruses in a standardized mouse model. *PLoS Negl Trop Dis* **16**, e0009845 (2022).
65. Cadd, T. L., Skoging, U. & Liljeström, P. Budding of enveloped viruses from the plasma membrane. *Bioessays* **19**, 993–1000 (1997).
66. Kaptur, P. E., Rhodes, R. B. & Lyles, D. S. Sequences of the Vesicular Stomatitis Virus Matrix Protein Involved in Binding to Nucleocapsids. *J Virol* **65**, 1057–1065 (1991).
67. Lyles, D. S. & Mckenzie, M. O. Articles Reversible and Irreversible Steps in Assembly and Disassembly of Vesicular Stomatitis Virus: Equilibria and Kinetics of Dissociation of Nucleocapsid-M Protein Complexes Assembled in Vivo. *Biochemistry* **37**, 439–450 (1997).
68. Newcomb, W. W. & Brown, J. C. Role of the Vesicular Stomatitis Virus Matrix Protein in Maintaining the Viral Nucleocapsid in the Condensed Form Found in Native Virions. *J Virol* **39**, 295–299 (1981).
69. Lyles, D. S., Mckenzie, M. & Parce, J. W. Subunit Interactions of Vesicular Stomatitis Virus Envelope Glycoprotein Stabilized by Binding to Viral Matrix Protein. *J Virol* **66**, 349–358 (1992).
70. Mebatsion, T., König, M. & Conzelmann, K.-K. Budding of Rabies Virus Particles in the Absence of the Spike Glycoprotein. *Cell* **84**, 941–951 (1996).
71. Hurley, J. H. & Hanson, P. I. Membrane budding and scission by the ESCRT machinery: It's all in the neck. *Nat Revs Mol Cell Biol* **11**, 556–566 (2010).
72. Colombo, M. *et al.* Analysis of ESCRT functions in exosome biogenesis, composition and secretion highlights the heterogeneity of extracellular vesicles. *J Cell Sci* **126**, 5553–5565 (2013).
73. Hurley, J. H. & Emr, S. D. The ESCRT complexes: Structure and mechanism of a membrane-trafficking network. *Annu Rev Biophys Biomol Struct* **35**, 277–298 (2006).
74. Garrus, J. E. et al. Tsg101 and the vacuolar protein sorting pathway are essential for HIV-1 budding. *Cell* **107**, 55–65 (2001).
75. Urata, S. *et al.* Interaction of Tsg101 with Marburg Virus VP40 Depends on the PPPY Motif, but Not the PT/SAP Motif as in the Case of Ebola Virus, and Tsg101 Plays a

Critical Role in the Budding of Marburg Virus-Like Particles Induced by VP40, NP, and GP. *J Virol* **81**, 4895–4899 (2007).

76. Timmins, J. *et al.* Ebola virus matrix protein VP40 interaction with human cellular factors Tsg101 and Nedd4. *J Mol Biol* **326**, 493–502 (2003).
77. Zhang, Y. *et al.* Proteomic Profiling of Purified Rabies Virus Particles. *Virol Sin* **35**, 143–155 (2020).
78. Wirblich, C. *et al.* PPEY Motif within the Rabies Virus (RV) Matrix Protein Is Essential for Efficient Virion Release and RV Pathogenicity. *J Virol* **82**, 9730–9738 (2008).
79. Itakura, Y. *et al.* Glu_{333} in rabies virus glycoprotein is involved in virus attenuation through astrocyte infection and interferon responses. *iScience* **25**, 104122 (2022).
80. Sabino, C., Bender, D., Herrlein, M. L. & Hildt, E. The epidermal growth factor receptor is a relevant host factor in the early stages of the Zika virus life cycle in vitro. *J Virol* **95**, e01195-21 (2021).
81. Anindita, P. D. *et al.* Ribavirin-related compounds exert in vitro inhibitory effects toward rabies virus. *Antiviral Res* **154**, 1–9 (2018).
82. Noda, T. *et al.* Ebola Virus VP40 Drives the Formation of Virus-Like Filamentous Particles Along with GP. *J Virol* **76**, 4855–4865 (2002).
83. Leis, J., Luan, C.-H., Audia, J. E., Dunne, S. F. & Heath, C. M. Ilaprazole and Other Novel Prazole-Based Compounds That Bind Tsg101 Inhibit Viral Budding of Herpes Simplex Virus 1 and 2 and Human Immunodeficiency Virus from Cells. *J Virol* **95**, e00190-21 (2021).
84. Park, A. *et al.* Nipah Virus C Protein Recruits Tsg101 to Promote the Efficient Release of Virus in an ESCRT-Dependent Pathway. *PLoS Pathog* **12**, e1005659 (2016).
85. Tabata, K. *et al.* Unique Requirement for ESCRT Factors in Flavivirus Particle Formation on the Endoplasmic Reticulum. *Cell Rep* **16**, 2339–2347 (2016).
86. Justice, P. A. et al. Membrane vesiculation function and exocytosis of wild-type and mutant matrix proteins of vesicular stomatitis virus. *J Virol* **69**, 3156–3160 (1995).
87. Chen, B. J. & Lamb, R. A. Mechanisms for enveloped virus budding: Can some viruses do without an ESCRT? *Virology* **372**, 221–232 (2008).
88. Irie, T., Licata, J. M., McGettigan, J. P., Schnell, M. J. & Harty, R. N. Budding of PPxY-Containing Rhabdoviruses Is Not Dependent on Host Proteins TGS101 and VPS4A. *J Virol* **78**, 2657–2665 (2004).
89. Pornillos, O. *et al.* Structure and functional interactions of the Tsg101 UEV domain. *EMBO J* **21**, 2397–2406 (2002).
90. Nickerson, D. P., Russell, M. R. G. & Odorizzi, G. A concentric circle model of multivesicular body cargo sorting. *EMBO Rep* **8**, 644–650 (2007).
91. Ferraiuolo, R. M., Manthey, K. C., Stanton, M. J., Triplett, A. A. & Wagner, K. U. The

multifaceted roles of the tumor susceptibility gene 101 (TSG101) in normal development and disease. *Cancers* **12**, (2020).

92. Strous, G. J. & Govers, R. The ubiquitin-proteasome system and endocytosis. *J Cell Sci* **112**, 1417–1423 (1999).
93. Harty, R. N., Paragas, J., Sudol, M. & Palese, P. A proline-rich motif within the matrix protein of vesicular stomatitis virus and rabies virus interacts with WW domains of cellular proteins: implications for viral budding. *J Virol* **73**, 2921–2929 (1999).
94. Sette, P., Jadwin, J. A., Dussupt, V., Bello, N. F. & Bouamr, F. The ESCRT-associated protein Alix recruits the ubiquitin ligase Nedd4-1 to facilitate HIV-1 release through the LYPX$_n$L L domain motif. *J Virol* **84**, 8181–8192 (2010).
95. Harty, R. N. *et al.* Rhabdoviruses and the Cellular Ubiquitin-Proteasome System: a Budding Interaction. *J Virol* **75**, 10623–10629 (2001).
96. Yasuda, J., Nakao, M., Kawaoka, Y. & Shida, H. Nedd4 Regulates Egress of Ebola Virus-Like Particles from Host Cells. *J Virol* **77**, 9987–9992 (2003).

Summary in Japanese

研究の背景

狂犬病ウイルス（RABV）によって引き起こされる狂犬病は、ヒトを含む幅広い哺乳類動物で致死的な神経症状を示す人獣共通感染症で、150 以上の国や地域に分布する。発症予防に有効なワクチンが存在する一方、有効な治療法が確立されていない。一度狂犬病を発症すると死を免れることは難しく、アジアやアフリカの貧困層を中心に死亡者数は毎年約 6 万人と推定される。公衆衛生学上、世界的に重要視される感染症であるにも関わらず、狂犬病の発生状況は改善していない。この背景には、予防薬および治療薬の開発研究の基盤となる RABV の病原性発現機構や感染増殖機構に関する知見の不足という現状がある。したがって本研究では、RABV の病原性ならびに感染・増殖機構の解明に取り組んだ。

第一章 G タンパク質の 333 位のアミノ酸に規定されるアストロサイト感染と IFN 応答による狂犬病ウイルスの弱毒化機構

RABV は、G タンパク質の 333 位（G333）のアミノ酸にグルタミン（Q）を保有することで病原性が低下することが知られている。弱毒化の例として G333 に Q をもつワクチン株 HEP は、マウスで神経症状を呈さないが、G333 をアルギニン（R）に置換した $HEP^{333}R$ 株は、マウスに致死的な病原性を示すようになる。第一章では、HEP 株とリバースジェネティクス法で作出した $HEP^{333}R$ 株の比較解析により、G333 に依存する病原性規定因子を探索した。

HEP 株と $HEP^{333}R$ 株を、神経細胞由来の NA 細胞とアストロサイト由来の SVG-A 細胞に感染させ、細胞の培養上清のウイルス力価測定により増殖効率を比較した。その結果、NA 細胞において両株は同等の増殖レベルを示した一方で、SVG-A 細胞においては、$HEP^{333}R$ 株が HEP 株に比べて低い増殖性を示した。アストロサイトにおける増殖性は、初代培養細胞においても同様の傾向を認め、$HEP^{333}R$ 株は HEP 株よりもアストロサイトへの親和性が低いことが示唆された。続いて、マウスにおけるアストロサイトへの感染性と IFN 産生の違いについて調べるために、HEP 株と $HEP^{333}R$ 株を感染させたマウスの脳からアストロサイトを分離し、ウイルスのゲノム量及びインターフェロン（IFN）の遺伝子発現量を qRT-PCR で評価した。その結果、$HEP^{333}R$ 株は HEP 株に比べて脳全体での増殖効率に対するアストロサイトへの感染効率が低かった。アストロサイトは脳内において IFN の主要産生細胞と考えられているが、$HEP^{333}R$ 株はアストロサイトでの IFN 産生レベルも低いことが明らかとなった。

既報の通り、免疫健常マウスを用いた感染実験では、HEP 株感染マウスは生存率

100%であったのに対し、HEP^{333}R 株感染マウスは神経症状を示し全例エンドポイントに達した。HEP 株は、HEP^{333}R 株よりも脳内のウイルス力価が有意に低いにも関わらず、IFN や ISGs 遺伝子の発現量は、HEP^{333}R 株と同等であった。続いて、HEP 株の弱毒化に対する IFN の影響を明らかにするために、I 型及び II 型 IFN 受容体欠損マウス（AG129 マウス）を用いて感染実験を実施した。その結果、HEP 株は全例において HEP^{333}R 株と同等の致死的病原性を発揮したことより、HEP 株の弱毒化には IFN が寄与することが示唆された。

以上の実験結果より、第一章では、G333 に依存した RABV の病原性の違いには、アストロサイト感染亢進による IFN 産生とそれに続く抗ウイルス活性の違いが関与することが明らかになった。

第二章 ESCRT タンパク質構成因子 TSG101 依存的な狂犬病ウイルスの出芽と弾丸状ウイルス粒子形成機構

RABV が有するウイルスタンパク質はわずか５種類であり、その機能も限られることから、ウイルスの感染増殖サイクルの遂行には多数の宿主因子の関与が予想される。しかしながら、RABV 感染に関与する宿主因子の知見は限られ、RABV の感染増殖機構には未解明な点が多い。第二章では、脂質膜の調節や切り離しを担う宿主の ESCRT（endosomal sorting complex required for transport）因子に着目し、RABV 感染増殖に関与する宿主因子の探索および機能解析を実施した。

まず、ESCRT 遺伝子群を標的とした siRNA スクリーニングにより、RABV 感染増殖に関与する宿主因子として ESCRT-I 構成因子の TSG101（tumor susceptibility gene 101 protein）を同定した。TSG101 は、late (L)-ドメインを介し RABV のマトリックスタンパク質（M）と相互作用した。L-ドメインは様々なウイルス間で保存され、ウイルス感染後期過程に機能するアミノ酸配列モチーフからなる。RABV の株間でも、L-ドメインは広く保存され、固定毒強毒株の CVS 株、固定毒弱毒株の HEP 株、街上毒株の Toyohashi 株は、TSG101 の発現抑制により、同様にウイルス産生量が低下した。RABV M が有する L-ドメインは、PY 及び YL モチーフから構成され、TSG101 との相互作用には、YL モチーフが強く関与することが明らかとなった。また、YL モチーフを置換した RABV 変異体は、細胞での増殖性及びマウスにおける病原性が低下し、ウイルスタンパク質の細胞内凝集及びウイルス粒子の弾丸型形状の破綻を認めた。これらの性状の異常は、TSG101 発現抑制細胞における親株ウイルス感染下でも共通して認められた。

以上の実験結果より、第二章では、RABV の出芽過程及び弾丸状ウイルス粒子形成が宿主 TSG101 依存的であり、本過程には、YL モチーフを介した RABV M−TSG101 相互作用が重要であることが示唆された。

総括

本研究は、第一章ではウイルス因子側から、第二章では宿主因子側からアプローチすることにより、RABV の新たな病原性発現（弱毒化）機構、ならびに出芽・弾丸状粒子形成の分子機序を提唱した。狂犬病の流行を阻止するためには、RABV を野犬の集団内で制御することが求められるが、野犬や野生動物用に使用される生ワクチンの作製には、ウイルスの病原性を規定する機序を理解することが重要となる。また、ウイルス–宿主間相互作用の理解は、自身の増殖に宿主を必須とするウイルスの感染環を理解する上で必至である。これらの研究が、RABV 感染の分子基盤解明に向けた更なる研究を促進し、今後の研究成果が狂犬病の新規治療法開発へとつながることが期待される。